Year-long, broad-band, microwave backscatter observations of an Alpine Meadow over the Tibetan Plateau with a ground-based scatterometer

Jan G. Hofste[1], Rogier van der Velde[1], Jun Wen[2], Xin Wang[3], Zuoliang Wang[3], Donghai Zheng[4], Christiaan van der Tol[1], and Zhongbo Su[1]

[1]Faculty of Geo-Information Science and Earth Observation (ITC), University of Twente, Enschede, Netherlands
[2]College of Atmospheric Sciences, Plateau Atmosphere and Environment Key Laboratory of Sichuan Province, Chengdu University of Information Technology, Chengdu, China
[3]Key laboratory of Land Surface Process and Climate Change in Cold and Arid Regions, Northwest Institute of Eco-Environment and Resources, Chinese Academy of Sciences, Lanzhou, China
[4]National Tibetan Plateau Data Center, Institute of Tibetan Plateau Research, Chinese Academy of Sciences, Beijing, China

Correspondence: Jan Hofste (j.g.hofste@utwente.nl)

Abstract. A ground-based scatterometer was installed on an alpine meadow over the Tibetan Plateau to study the soil moisture and -temperature dynamics of the top soil layer and air–soil interface during the period August 2017 – August 2018. The deployed system measured the amplitude and phase of the ground surface radar return at hourly and half-hourly intervals over $1 - 10$ GHz in the four linear polarization combinations (vv, hh, hv, vh). In this paper we describe the developed scatterometer system, gathered datasets, retrieval method for the backscattering coefficient (σ^0), and results of σ^0 for co-polarization.

The system was installed on a 5 m high tower and designed using only commercially available components: a Vector Network Analyser (VNA), four coaxial cables, and two dual polarization broadband gain horn antennas at a fixed position and orientation. We provide a detailed description on how to retrieve the co-polarized backscattering coefficients σ^0_{vv} & σ^0_{hh} for this specific scatterometer design. To account for the particular effects caused by wide antenna radiation patterns (G) at lower frequencies, σ^0 was calculated using the narrow-beam approximation combined with a mapping the function G^2/R^4 over the ground surface. (R is the distance between antennas and the infinitesimal patches of ground surface.) This approach allowed for a proper derivation of footprint positions and -areas, and incidence angle ranges. The frequency averaging technique was used to reduce the effects of fading on the σ^0 uncertainty. Absolute calibration of the scatterometer was achieved with measured backscatter from a rectangular metal plate as reference target.

In the retrieved time-series of σ^0_{vv} & σ^0_{hh} for S-band ($2.5 - 3.0$ GHz), C-band ($4.5 - 5.0$ GHz), and X-band ($9.0 - 10.0$ GHz) we observed characteristic changes or features that can be attributed to seasonal or diurnal changes in the soil. For example a fully frozen top soil, diurnal freeze-thaw changes in the top soil, emerging vegetation in spring, and drying of soil. Our preliminary analysis on the collected σ^0 time-series data set demonstrates that it contains valuable information on water- and energy exchange directly below the air-soil interface. Information which is difficult to quantify, at that particular position, with in-situ

measurements techniques alone.

Availability of backscattering data for multiple frequency bands allows for studying scattering effects at different depths
within the soil and vegetation canopy during the spring and summer periods. Hence further investigation of this scatterometer
data set provides an opportunity to gain new insights in hydro-meteorological processes, such as freezing and thawing, and how
these can be monitored with multi-frequency scatterometer observations. The data set is available via https://doi.org/10.17026/dans-
zc5-skyg (Hofste and Su, 2020)

The effects of fading, calibration, and system stability on the uncertainty in σ^0 are estimated to vary from $\pm$ 1.3 dB for
X-band with vv-polarization to $\pm$ 2.7 dB for S-band with hh-polarization through the campaign. The low angular resolution of
the antennas result in additional σ^0 uncertainty, one that is more difficult to quantify. Estimations point out that it probably will
not exceed $\pm$ 2 dB with C-band. Despite these uncertainties, we believe that the strength of our approach lies in the capability
of measuring σ^0 dynamics over a broad frequency range, 1 – 10 GHz, with high temporal resolution over a full-year period.

1   Introduction

For accurate climate modelling of the Tibetan Plateau, also known as the 'third pole environment', the transfer processes of
energy and water at the land-atmosphere interface must be understood (Seneviratne et al., 2010), (Su et al., 2013). Main quan-
tities of interest are the dynamics of soil moisture and -temperature (Zheng et al., 2017a). Together with sensors embedded into
the deeper soil layers, microwave remote sensing is suitable to study these dynamics since it directly probes the top soil layer
within the antenna footprint.

A ground-based microwave observatory was installed on an alpine meadow over the Tibetan plateau, near the town of Maqu
(China). The observatory consists of a (passive) microwave radiometer system called ELBARA-III (ETH L-Band radiometer
for soil moisture research) (Schwank et al., 2010), (Zheng et al., 2017b), and an (active) microwave scatterometer. Both contin-
uously measure the surface's microwave signatures with a temporal frequency of once every hour year round. The ELBARA-III
was installed in January 2016 and is currently still measuring (Su et al., 2020), the scatterometer was installed in August 2017
and continued to operate until July 2019.

This paper describes the scatterometer system and the dataset that has been collected over the period August 2017 – August
2018 (Hofste and Su, 2020). The scatterometer was built with commercially available components: a vector network analyser

(VNA), four phase stable coaxial cables, two dual polarization broadband gain horn antennas, and a laptop controlling the scatterometer's operation autonomously. The radar return amplitude and phase were measured over a broad 1- 10 GHz frequency

55 band at all four linear polarization combinations (vv, hv, vh, hh). In this paper the co-polarizations results shall be discussed. The scatterometer measured the radar return over a prolonged time with its antennas in a fixed position and orientation, resulting in frequency-dependent incidence angle ranges varying from of $20° \leq \theta \leq 65°$ for L-band (1.25 GHz) to $47° \leq \theta \leq 59°$ for X-band (9.5 Ghz). During the summers of 2017 and 2018 additional experiments were conducted to asses the angular dependence of the backscatter and homogeneity of the local ground surface.

60

Many other studies exist employing ground-based systems to study microwave backscatter from land. Rather than an airborne- or spaceborne system, ground-based systems allow for high temporal resolution coverage and a high degree of control over the experimental circumstances. Geldsetzer et al. (2007) and Nandan et al. (2016) use specially developed radar systems by ProSensing Inc. to study backscattering from sea ice in the period 2004 - 2011: one system for C- and another

65 for X- & Ku-band. Details on a similar system for S-band can be found in Baldi (2014). The SnowScat system, developed by Gamma Remote Sensing AG (Werner et al., 2010), is another specifically designed scatterometer that operates over 9 - 18 GHz and measures the full polarimetric backscatter autonomously over many elevation- and azimuth angles. SnowScat was used during multiple winter campaigns in the 2009 - 2012 period at two different locations to study the scattering properties of snow layers (Lin et al., 2016). Like in this study, others also designed their scatterometer architecture around a commercially

70 available VNA. For instance, (Joseph et al., 2010) used data measured by a truck-based system, operating at C- and L-band, in the 2002 summer to study the influence of corn on the retrieval of soil moisture from microwave backscattering. For every band they placed one antenna for transmit and receive on top of a boom. Selection of the individual polarization channels was realized using RF switches. Similar is the University of Florida L-band Automatic Radar System (UF-LARS) (Nagarajan et al., 2014), used by, for example Liu et al. (2016), to measure soil moisture at L-band from a Genie-platform during the

75 2012 summer. Another example is the Hongik Polarimetric Scatterometer (HPS) (Hwang et al., 2011), with which microwave backscatter from bean- and corn fields was measured in 2010 and 2013 respectively (Kweon and Oh, 2015). Similar to our study, Kim et al. (2014) used a scatterometer with its antenna in a fixed position and orientation to measure the backscattering during all growth stages of winter wheat at L-, C- and X-band during 2011 - 2012.

80 The temporal resolution and measurement period covered by the scatterometer data set reported in this paper permits studying both seasonal- and diurnal dynamics of microwave backscattering from an Alpine meadow ecosystem. This in turn allows for investigating the local soil moisture content dynamics, the freeze-thaw process, and growth/decay stages of vegetation. Because of the broad frequency range measured (1 – 10 GHz), wavelength-dependent effects of surface roughness and vegetation scattering can be studied as well.

85

This paper is organized as follows. First, details on the measurement site and present instruments are given. Followed by details on the scatterometer instrumentation, -setup, -geometries, and -calibration, along with a description of all performed

experiments. Next the calculation method for the backscattering coefficient, or normalized radar cross section, σ^0 is described. Given the system's configuration we show what assumptions and approximation were made for calculating σ^0 from the measured radar return amplitude- and phase data. We then show some measurement results of σ^0. These are the angular response of σ^0 for asphalt, experiments to explore the angular and spatial variability of σ^0 at the measurement site, and finally some results of the time-series of σ^0. A list of used symbols can be found at the end of this paper.

2 Measurement site

2.1 Maqu site

In August 2017 the scatterometer was installed on the tower of the Maqu measurement site (Maqu site) (Zheng et al., 2017b), and operated over the period August 2017 – June 2019. The Maqu site is situated in an Alpine meadow ecosystem (Miller, 2005) on the Tibetan plateau. The site's coordinates are $33°55'$ N, $102°10'$ E, at $3500\,\mathrm{m}$ elevation. The site is located close to the town Maqu of the Gansu province of China.

Besides the scatterometer, other remote sensing sensors placed on the tower are the ELBARA-III radiometer (Schwank et al., 2010) and the optical spectroradiometer system 'Piccolo' (MacArthur et al.), see Fig. 1. The ELBARA-III system has been measuring L-band microwave emission from January 2016 to this date (Su et al., 2020). The Piccolo system measured the reflectance and sun-induced chlorophyll fluorescence of the vegetation over the period July - November 2018.
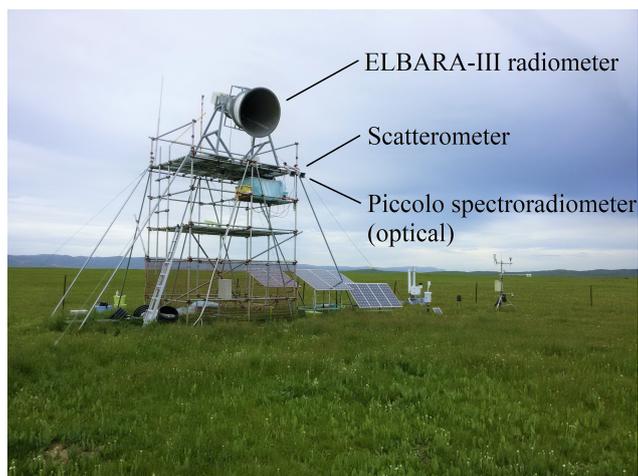
Figure 1. Tower of Maqu site containing the scatterometer, the ELBARA-III radiometer, and Piccolo optical spectroradiometer.

2.2 Climate

According to Peel et al. (2007) the climate at Maqu is characterized by the Köppen-Geiger classification as 'Dw', Cold with dry winters. Winter (December - February) and spring (March - May) are cold and dry while the summer (June - August) and

Table 1. Measured vegetation parameters at Maqu-site during summer 2018

	12 July 2018	17 August 2018
Height (distribution max.) (cm)	25	40
Biomass Fresh (Kgm^{-2})	0.9	1.3
Biomass Dry (Kgm^{-2})	0.3	0.5
VWC (%)	60	62
LAI (m^2m^{-2})	3.5	7

autumn (August - November) are mild with monsoon rain. Over 2018, during the coldest period in January the diurnal air temperature varied from -24 °C to -3 °C while in summer, during the warmest period in August the diurnal air temperature varied from 8 °C to 18 °C. The top soil temperature drops below 0 °C in- and around the winter period, while from mid spring to mid autumn soil temperature at all depths remain above this temperature. Measurements with the thermistors of the 5TM sensor array showed that during the 2018 winter the soil temperature dropped below 0 °C up to a depth of 70 cm. From August 2017 to July 2018 the precipitation per season was: 419 mm in autumn, 2 mm in winter, 41 mm in spring, and 128 mm in summer.

2.3 Vegetation

The ecosystem classification of the Maqu site is Alpine Meadow according to Miller (2005). The vegetation around the Maqu site consists for a major part of grasses. The growing season starts at the end of April and ends in October, when above-ground biomass turns brown and loses its water. During the growing season the meadows are regularly grazed by lifestock. To prevent this lifestock from entering the site and damaging the equipment a fence is placed around the Maqu site. As a result there is no grazing within the site, causing the vegetation to be more dense and higher than that of the surroundings. Also a layer of dead plant material from the previous year remains present below the newly emerged vegetation.

To quantify the vegetation cover at the Maqu site, a set of measurements were performed on two days during the 2018 summer: 12 July and 17 August. Vegetation height, above-ground biomass (fresh & over-dried), and leaf area index (LAI) were measured at ten 1.2×1.2 m^2 sites around the periphery of the no-step zone indicated in Fig. 2. The average quantities over the ten sites are summarized in Table 1. The vegetation height of a single site was determined as the maximum value of the histogram obtained by taking ≥ 30 readings with a thin ruler at random points within the site area. For each site above-ground biomass and LAI were determined from harvested vegetation within one or two disk areas defined by a 45 cm diameter ring. Immediately after harvest all biomass was placed in air-tight bags so that the fresh- and dry biomass could be determined by weighing the bag's content before and after heating with an oven. The LAI was determined immediately after harvest with part of the harvested fresh biomass by the plotting method described in He et al. (2007).
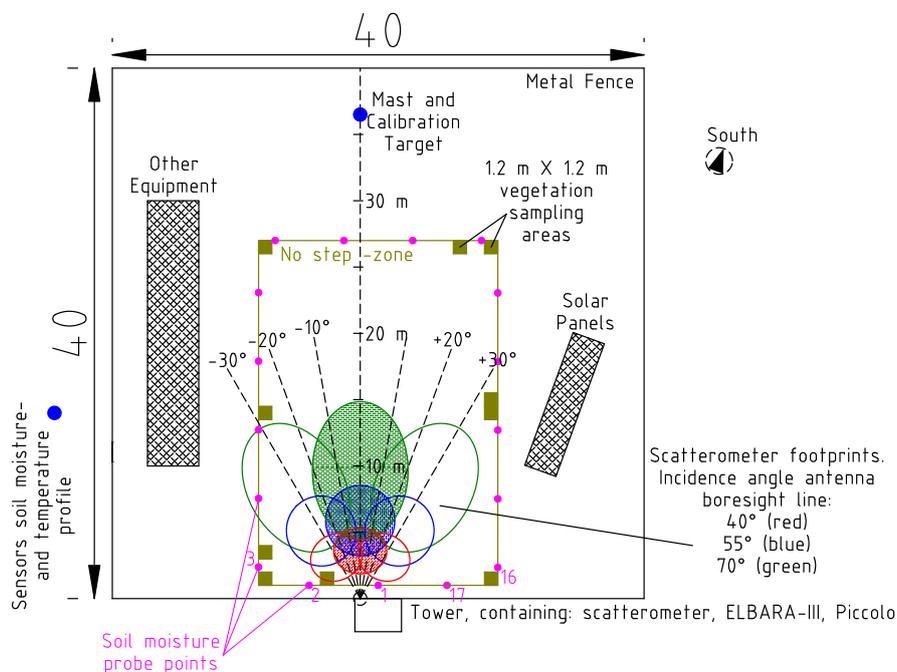
Figure 2. Map of the Maqu site. Scatterometer footprints for C-band with vv polarization shown for different incidence angles of antenna boresight line: $\alpha_0 = 40, 55, 70°$. Also shown are antenna azimuth angles ϕ.

2.4 Hydrometeorological sensors

Table 2 lists all hydrometeorological instruments used for this study along with their reported measurement uncertainties. Air temperature was measured with a Platinum resistance thermometer, type HPM 45C, installed 1.5 m above the ground and precipitation (both rain and snow) was measured with a weight-based rain gauge, type T-200B. The depth profile of volumetric

Table 2. Overview of relevant Hydrometeorological sensors Maqu site

Quantity	Type, Manufacturer:	Unit, Uncertainty:
Volumetric soil moisture content m_v	5TM, Meter Group	$\pm 0.02 \, \mathrm{m^3 m^{-3}}$ (Zheng et al., 2017b)
Volumetric soil moisture content m_v	ThetaProbe ML2x, Delta-T Devices	$\pm 0.05 \, \mathrm{m^3 m^{-3}}$
Soil temperature	5TM, Meter Group	$\pm 1 \, \mathrm{°C}$
Air temperature	HPM 45C, Campbell Scientific	$\pm 1 \, \mathrm{°C}$
Precipitation (rain & snow)	T-200B, Geonor	$\pm 0.6 \, \mathrm{mm}$

135   soil moisture content m_v ($\mathrm{m^3 m^{-3}}$) was measured with an array of 20 capacitance sensors, type 5TM, that were installed at depths ranging from 2.5 cm to 1 m (Lv et al., 2018). All sensors in the array are also equipped with a thermistor, enabling the measurement of the soil temperature depth profile T_{soil} (°C). The soil moisture and -temperature was logged every 15 minutes

for the period of August 2017 – August 2018 with Em50 data loggers (manufacturer: Meter Group) that were buried nearby with the sensors. The location of the buried sensor array is indicated in Fig. 2.

140

We estimate that the spatial average top soil moisture content over the Maqu site M_v ($\mathrm{m}^3\mathrm{m}^{-3}$) is linked to m_v as measured by the 5TM sensors at 2.5 and 5 cm depth (m_v^{5TM}) according to

$$M_v = m_v^{5TM} \pm S_{tot} \tag{1}$$

where S_{tot}, with value 0.04 $\mathrm{m}^3\mathrm{m}^{-3}$, is the total standard deviation of spatially measured m_v with a hand held impedance

145 probe, type ThetaProbe ML2x. Refer to Appendix A for additional information.

3 Scatterometer and its operation

3.1 Instrumentation

The main components of the scatterometer are a 2-port vector network analyser (VNA), type PNA-L 5232A (manufacturer: Keysight), four 3 m long phase stable coax cables, type Succoflex SF104PEA (manufacturer Huber + Suhner), and two dual

150 polarization broad band horn antennas, type BBHX9120LF (manufacturer: Schwarzbeck). The test port couplers of the VNA are removed and the coax cables are connected according to the schematic in Fig. 3. This configuration allows for measuring
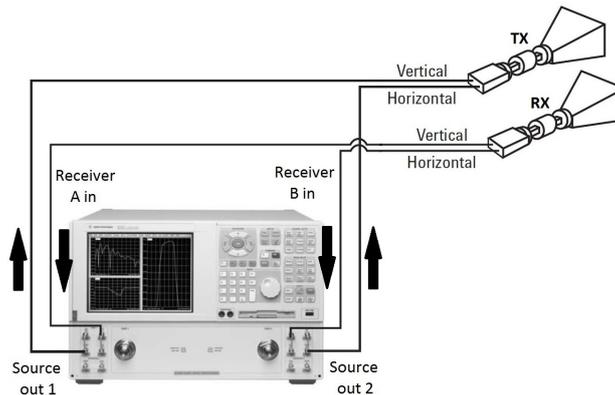
Figure 3. Connection scheme of scatterometer. Both dual polarization antennas, one for transmitting (TX) both polarizations and the other for receiving (RX) both polarizations, are connected to the VNA as indicated. Arrows indicate direction of signal.

all four polarization channels: vv (transmit in vertical direction, receive in vertical direction), vh, vh, and hh. Between all four coaxial cables and their respective VNA connectors 10 dB attenuators, type SMA attenuator R411.810.121 (manufacturer: Radiall) were inserted to prevent interference from internal reflections travelling multiple times up- and down the coaxial cables.

155 To protect the VNA from weather it is placed inside a water proof enclosure equipped with fans to provide air ventilation. The antenna radiation patterns are measured in the principal planes by the manufacturer over the 1 – 10 GHz band (Schwarzbeck

Mess-Elektronic, 2017). As a summary, the full width half max (FWHM) intensity beamwidths over frequency are shown in Appendix C, Fig. C1. The scatterometer is placed on a tower as shown in Fig. 1. The two antenna apertures are at a distance approximate $H_{ant} = 5$ m above the ground (H_{ant} depends on the antenna boresight angle α_0) and are separated from each other horizontally by $W_{ant} = 0.4$ m.

Deployed reference targets to calibrate the scatterometer, and subsequently validate this calibration, were a rectangular plate and two dihedral reflectors. The rectangular plate reflector was constructed from light-weight foam board covered with $100\,\mu$m aluminium foil and had frontal dimensions $a = 85\,\mathrm{cm} \times b = 65\,\mathrm{cm}$. A small dihedral reflector was constructed from steel, its frontal dimensions were $a = 57\,\mathrm{cm} \times b = 38\,\mathrm{cm}$. A second large dihedral reflector was also constructed with foam board and aluminium foil, its frontal dimensions were $a = 120\,\mathrm{cm} \times b = 65\,\mathrm{cm}$. A height-adjustable metal mast was used to position the reference targets. To minimize reflection from this mast it was covered by pyramidal absorbers, type 3640-300 (manufacturer: Holland Shielding), having a 35 dB reflection loss at 1 GHz under normal incidence.

3.2 Setup

Figure 4 shows all relevant geometries for the experiments performed. The two antenna apertures are at distance H_{ant} above the ground surface. The separation between the two antenna apertures $W_{ant} = 0.4$ m is small compared to the target distance (ground or calibration standards) which justifies using the geometric centre of the two apertures for all calculations. Every area segment dA (m^2) of the ground surface has its own distance to the antennas R and angle of incidence θ. Angles α and β are angular coordinates of R. Angle α is defined between the tower's vertical axis and the orthogonal projection of the line from antennas to a ground surface segment onto the plane formed by the tower's vertical axis and the antenna boresight direction line. Angle β is defined between line from antennas to a ground surface segment and projection of that same line onto the plane formed by the tower's vertical axis and the antenna boresight direction line. The planes in which α and β lie are also the antenna's principal planes (see for example (Balanis, 2005)). For the antenna boresight direction $\alpha = \alpha_0$ and $\beta = \beta_0$. The antenna rotation around the tower's vertical axis is defined as azimuth rotation ϕ.

According to Bansal (1999) the antenna's far field distances R_{ff} (m) are linked to the antenna's largest aperture dimension D (m) and wavelength λ via

$$R_{ff} \geq \begin{cases} 5D & : \frac{1}{3} \leq \frac{D}{\lambda} \leq \frac{5}{2} \\ \frac{2D^2}{\lambda} & : \frac{5}{2} < \frac{D}{\lambda} \end{cases} \tag{2}$$

The antenna aperture is rectangular with dimension $D = 0.2$ m, which leads to $R_{ff} \geq 1$ m for 1 - 3.5 GHz and $R_{ff} \geq 2.7$ m for 3.5 - 10 GHz. Given that with all measurements the distance to the ground surface is larger than 2.7 m the radiation patterns as measured by the manufacturer apply, (Schwarzbeck Mess-Elektronic, 2017).

Open Access   Earth System
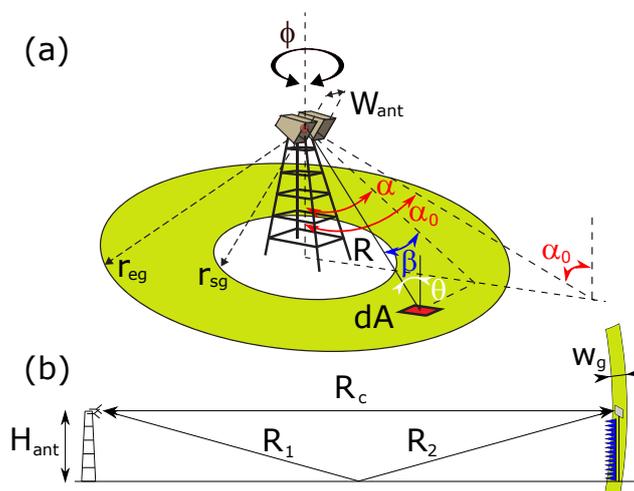
Figure 4. Schematic of scatterometer geometry. (a) Every infinitesimal area dA has its own distance R to the geometric centre between antenna apertures (red dot) and angle of incidence θ. Angles α and β lie within the antennas principal planes, α_0 denotes the angle of antenna boresight. The green ring is a projection of the spherical gating shell with radii r_{sg} and r_{eg} onto the ground. (b) Side view of geometry during measurement of reference standards. Green ring depicts cross section of spherical gating shell with width w_g.

The radar return from the rectangular metal plate reference target was used to calibrate the scatterometer for the co-polarization channels, as illustrated in Fig. 4(b). Radar returns from both metal dihedral reflectors were measured as well.

190   First, to enable calibration for cross polarization in the future, and second, to validate the co-polarization calibration by retrieving the dihedral reflector's radar cross sections (RCS) σ_{pp}. We worked with two dihedral reflectors, installed at different distances R_c to satisfy additional requirements. Refer to Appendix B for the measurement details and validation-exercise results.

195   Time-domain filtering, or gating, was used as part of post processing to remove the antenna-to-antenna coupling and undesired scattering contributions from the radar return signal for both the reference target- as the ground return measurements. The ring on the ground surface in Fig. 4 is the intersection of a spherical shell with radii r_{sg} and r_{eg} centred at the antennas and the ground surface. It represents the selected ground surface area for the gating algorithm: roughly put, scattering returns from features within the spherical shell remain in the radar return signal while those outside the shell are removed.

200   The application of gating with VNA-based scatterometers is described in more detail in for example (Jersak et al., 1992) or (De Porrata-Dória i Yagüe et al., 1998). Details on our gating process and related peculiarities regarding our scatterometer can be found in Appendix C.

3.3   Experiments

During all experiments, VNA measurements were performed with a stepped $0.75 - 10.25$ GHz frequency sweep at 3 MHz resolution (3201 points). The dwell time per measured frequency was 1 μs, equivalent to a two-way travelling distance for the microwave signal of 150 m. The intermediate-frequency (IF) bandwidth was minimized to 1 KHz to increase the signal-to-noise ratio.

In this paper, we describe the following experiments: a measurement of the σ^0 for asphalt at various α_0 angles, measurements of σ^0 for different α_0- and ϕ angles at the Maqu site, and finally the measurement of σ^0 over a one-year period. Table 3 summarizes the experiment geometries and dates of execution. With the angular-variation experiments the scatterometer antennas were mounted on a motorized rotational stage. Depending on the angle α_0, H_{ant} would vary according to $H_{ant} = H_0 - 0.5\cos(\alpha_0)$, with $H_0 = 2.95$ or 5.2 m for the asphalt- or Maqu experiments respectively. With the time-series experiment the antennas were fixed on a tower rod, such that α_0 was 55 °. All angular-variation experiments were conducted within one afternoon. With the time-series experiment the radar return was measured either once or twice per hour continuously.

Table 3. Overview scatterometer experiments

	Date:	ϕ (°):	α_0 (°):	H_{ant} (m):
Angular variation σ_0 asphalt	4 May 2017	00	35 40 .. 75	2.55 2.55 .. 2.80
Angular variation σ_0 Maqu	25 August 2017	-20 -15 -10 -05 00 +10 +15 +20	35 40 .. 70	4.80 4.80 .. 5.05
Angular variation σ_0 Maqu	29 June 2018	-30 -20 -15 -10 -05 00 +05 +10 +20 +25 +30	35 40 .. 70	4.80 4.80 .. 5.05
Angular variation σ_0 Maqu	19 August 2018	-30 -20 -10 00 +10 +20 +30	35, 55, 70	4.80 4.90 5.05
Time series σ_0 Maqu	26 August 2017 – 26 August 2018	00	55	4.70

4   Derivation of the backscattering coefficient

4.1   Effects of wide radiation patterns

The power received by a monostatic radar- or scatterometer system from a distributed target with backscattering coefficient $\sigma_{pq}^0(\theta)$ (m³m⁻³) is given by the radar equation

$$P_q^{RX} = \frac{\lambda^2}{64\pi^3} P_p^{TX} G_0^2 \int \frac{G^2}{R^4} \sigma_{pq}^0(\theta).dA \tag{3}$$

where it is assumed that the same antenna is used for both transmitting (TX) and receiving (RX). P_p^{TX} is the transmitted-, and P_q^{RX} the received power respectively (W). The subscripts of the powers refers to the linear polarization directions: horizontal h, or vertical v. With σ_{pq}^0 the first subscript refers to the polarization direction of the incident- and the second to that of the scattered wave. $G\ (-)$ denotes the normalized angular gain pattern of the antenna with peak value $G_0\ (-)$. Equation 3 represents an ideal lossless system, in practice any scatterometer has frequency dependent losses or other signal distortions. These frequency dependent phase- and amplitude modulations can be accounted for by measuring the radar return of a reference target P_q^c with known radar cross section σ_{pq} (m^2) (see Appendix. B) and subsequently using this to calibrate the system. This procedure is often referred to as external calibration. Substitution of terms associated with the reference measurement into Eq. 3 leads to

$$P_q^{RX} = P_q^c \frac{(R_c)^4}{\sigma_{pq}} \int \frac{G^2}{R^4} \sigma_{pq}^0(\theta).dA \tag{4}$$

where R_c (m) is the distance at which the reference target was measured. In the case of a scatterometer with narrow beamwidth antenna, all integrand terms of Eq. 4 can be approximated as being constants, the so-called 'narrow-beam approximation' (Wang and Gogineni, 1991), so that we obtain

$$P_q^{RX} = P_q^c \frac{(R_c)^4}{\sigma_{pq}} \frac{1}{(R_{fp})^4} \sigma_{pq}^0(\theta) A_{fp} \tag{5}$$

where A_{fp} is the scatterometers 'footprint', notably the area (m^2) for which the surface projected antenna beam intensity is equal to or larger than half its maximum value. R_{fp} (m) refers to the distance between the antenna and footprint centre.

For this dataset $\sigma_{pp}^0(\theta)$ is estimated by employing Eq. 5 in combination with a mapping of the term $G^2/R^4(x,y)$ from Eq. 4 over the ground surface. Due to the wide antenna radiation patterns, especially with low frequencies, the area that is to be associated with the measured scatterometer signal, i.e. the footprint is typically not located where the antenna boresight line intersects the ground surface. Instead the footprint appears closer to the tower base. Figure 5 demonstrates this effect for the case of 5 GHz at $\alpha_0 = 55\ °$. Shown is the mapping over the ground surface of the G^2/R^4 -term from Eq. 4. This footprint-shift effect is strongest with the widest antenna radiation patterns (thus with low frequencies) and for large α_0 angles. The footprint position and dimensions were found using the mapping $G^2/R^4(x,y)$ over the ground surface. The applied criterion was that the footprint contains 50% of the total projected intensity onto the ground surface. After the footprint edges were defined the incidence angle ranges were derived from them using straightforward trigonometry.

Because of the low angular resolution of the antennas and the unknown nature of σ_{pq}^0 over θ, there is an uncertainty in the absolute level of our retrieved σ_{pq}^0 values (for a certain θ range). Quantifying this uncertainty is outside the scope of this paper. In Sec. 5.1.2 we do however provide an estimate of what this uncertainty could be. Despite this flaw we show that nevertheless the temporal dynamics of σ_{pq}^0, for various wavelengths, can be measured with our system.
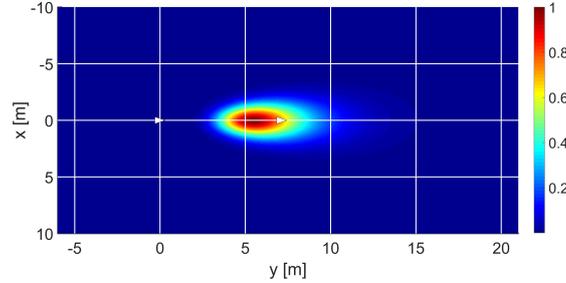
Figure 5. Example of $G^2/R^4(x,y)$ with Gaussian antenna radiation patterns. Plot normalized to its peak value. x and y are ground surface coordinates. White triangle at coordinate (0,0) represents the tower location and other white triangle indicates intersection point of the antenna boresight line and the ground surface. $\alpha_0 = 55°$, $f = 5$ GHz and polarization is vv.

4.2 Implementation of the radar equation

We rewrite Eq. 5 so that the backscattering coefficient of the surface σ^0 ($\mathrm{m^2 m^{-2}}$) is related to the average received backscattered intensity $\bar{I}$ ($\mathrm{Wm^{-1}}$) as (Ulaby and Long, 2017)

$$\sigma^0 = K^{-1}\bar{I} \tag{6}$$

where for brevity the polarization subscripts are omitted. The factor K ($\mathrm{Wm^{-1}}$) is a constant for the bandwidth considered given by

$$K = \frac{\lambda^2}{4\pi^3} I^t \frac{G^2}{R_{fp}^4} A_{fp} \tag{7}$$

where I^t ($\mathrm{Wm^{-1}}$) is the transmitted intensity by the scatterometer. For all terms in K the centre frequency is used. Similar as with Eq. 4, we can substitute I^t in Eq. 7 by the relevant radar parameters when a reference target is measured, yielding

$$K = c\epsilon_0 (E_c^{gc} - E_{bc}^{gc})^2 \frac{G(\alpha,\beta)^2}{G(\alpha_0,\beta_0)^2} \left(\frac{R_c}{R_{fp}}\right)^4 \frac{A_{fp}}{\sigma} = c\epsilon_0 (E_c^{gc} - E_{bc}^{gc})^2 \left(\frac{R_c}{R_{fp}}\right)^4 \frac{A_{fp}}{\sigma} \tag{8}$$

E_c^{gc} ($\mathrm{Vm^{-1}}$) is the measured backscattered field from the reference target (subscript c for 'calibration') and E_{bc}^{gc} ($\mathrm{Vm^{-1}}$) is the measured background level during calibration, i.e. the measured backscattered electric field when the calibration standard was removed from the mast while the pyramid absorbers remained in place. With both terms the superscript gc (for 'gate' during 'calibration') indicates that an identical gate was used. The prefactors light speed c ($\mathrm{ms^{-1}}$) and the permittivity of vacuum ϵ_0 ($\mathrm{CV^{-1}m^{-1}}$) convert the electric field strengths into time-average intensity. In the middle part of Eq. 8 the antenna gain functions are written explicitly. $G(\alpha,\beta)$ represents the antenna gain functions when measuring the ground return, while $G(\alpha_0,\beta_0)$ represents the situation when the radar return of the reference targets is measured. When using the narrow beam approximation (Eq. 5) and when the reference target is aligned to the antenna boresight direction the fraction becomes unity and the right part of Eq. 8 follows. The middle part is used in Appendix. D2 when alignment uncertainty of the reference targets is discussed.

In the context of Rayleigh fading statistics with square-law detection (Ulaby et al., 1988), the average received intensity $\bar{I}$ (Wm^{-2}) is linked to I_N (Wm^{-2}), which is the measured intensity averaged over N independent samples (N footprints or N frequencies), according to

275
$$\bar{I} = \frac{I_N}{1 \pm 1/\sqrt{N}} \qquad (9)$$

Note that $\bar{I}$, like σ^0 is an implied ground surface property. The quantity that is actually measured, I_N, is an estimator for $\bar{I}$. Equation 9 holds for $N \geq 10$, since then the probability density function of I_N approaches a Gaussian distribution (Ulaby et al., 1982) according to the central limit theorem. The denominator in Eq. 9 represents a 68% confidence interval (± 1 standard deviation) for $\bar{I}$. More details on fading are described in Section 4.3.

280

I_N is calculated from the measured backscattered electric field from the ground target incident on the receiving antenna E_e^g (Vm^{-1}) by

$$I_N = c\epsilon_0 \frac{1}{N} \sum_{i=1}^{N} (E_e^g(f_i) - E_n^g(f_i))^2 \qquad (10)$$

The subscript e denotes 'envelope' magnitude of the complex signal, as in (Ulaby et al., 1988)[1] and the superscript g indicates
285 that the signal is gated. E_n^g (Vm^{-1}) is the measured electric field with the antennas pointing skywards and thus represents the scatterometer's 'noise' level. Note that the exact gate is applied as with E_e^g.

4.3 Fading and bandwidth selection

Fading is the phenomena that radar return of a distributed target with uniform electromagnetic properties has varying magni-
290 tudes and phases when different locations or slightly different frequencies are measured (Ulaby et al., 1988), (Monakov et al., 1994). To remove this varying nature from a surface-classifying quantity like σ_{pq}^0 averaging must be performed. By definition σ_{pq}^0 is the average radar cross section of a certain type of distributed target, e.g. forest, asphalt, wheat field, normalized by the illuminated physical surface area. σ^0 is proportional to the average measured received power P^{RX} (Eq. 5) or intensity $\bar{I}$. Therefore, determining $\bar{I}$ and σ^0 requires N statistically independent samples so that the sample average I_N approaches the
295 actual average $\bar{I}$ proportionally to $1/\sqrt{N}$ in accordance with the central limit theorem.

Practically, this can be done either by measuring I at N different locations over the surface, called spatial averaging, or with the frequency averaging -technique (see for example (Ulaby et al., 1988)). With the latter, physical properties governing the scattering, permittivity and surface roughness are considered frequency invariant over a certain bandwidth. Subsequently, N
300 different frequencies should be selected according to some criteria that accounting for fading. Both averaging techniques can be used simultaneously as done by Nagarajan et al. (2014) to increase the total number of independent samples. We solely

---

[1]In reality the measured fields or signals remain complex until after the gating process. We however stick to this terminology for clarity.

applied the frequency-averaging technique because during the time-series measurements our antennas were in a fixed position and orientation. We assumed the single footprint area to be representative for the whole surface of the Maqu site. In Sec. 5.2.2 we show this assumption is justified. The used method for finding the number N of statistically independent samples within a bandwidth is described in Mätzler (1987):

$$N = \frac{2BW\Delta R}{c} \tag{11}$$

where $\Delta R = r_{sg} - r_{eg}$. Subsequently, with $N-1$ intervals of Δf (Hz), N frequencies are selected from within BW.

As indicated above, with the application of the frequency averaging technique it is assumed that the backscatter behaviour across the selected BW is uniform. To assess the validity of this assumption for bare surface, the improved integral equation method (I^{2}EM) surface scattering model (Fung et al., 2002) is applied using the roughness parametrization reported in Dente et al. (2014) and a (frequency dependent) effective dielectric constant $\epsilon_{soil}(f)$ according to the dielectric mixing model by Dobson et al. (1985).

Over a BW the mean value $\langle \sigma^0(BW) \rangle$ is calculated, followed by the ratios $\sigma^0(BW_{lo})/\langle \sigma^0(BW) \rangle$ and $\sigma^0(BW_{hi})/\langle \sigma^0(BW) \rangle$ to quantify the change of σ^0 over the BW. In general the I^{2}EM model predicts that the change is largest for long- and smallest for short wavelengths and that it is largest for hh polarization and smallest for vv polarization. Furthermore, the RMS surface height is the most sensitive target parameter. As an example, figure 6 shows the calculation result for hh polarization with a
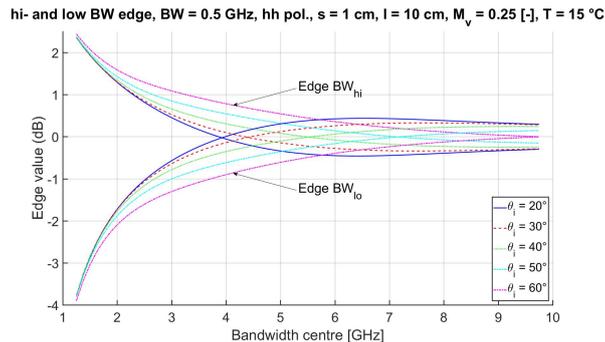
Figure 6. Variation of σ^0_{hh} per BW calculated with combined I^{2}EM- (Fung et al., 2002) and Dobson (Dobson et al., 1985) model. Horizontal axis shows centre frequency of bandwidth $BW = 0.5\,\text{GHz}$. Curves indicate the values (in dB) to be added to $\langle \sigma^0_{hh}(BW) \rangle$ at edges of BW for different θ angles. Shown calculation uses: $s = 1\,\text{cm}$, $\ell = 10\,\text{cm}$, $m_v = 0.25\,\text{m}^3\text{m}^{-3}$, and $T_{soil} = 15\,°\text{C}$.

BW of 0.5 GHz. From the graph we can read that for a centre frequency of 2.75 GHz that the retrieved σ^0_{hh} for that BW can be expected to vary $+1.0$ to -1.2 dB for $\theta = 50°$.

Based on the above calculations we chose $BW = 0.5\,\text{GHz}$ for S-, and C-band and $BW = 1.0\,\text{GHz}$ for X-band. These bandwidths will lead to N-values around 15 which is sufficient to let the probability density function of I_N approach a

Gaussian distribution. as explained in Sec. 4.4. Further increment of BW was considered not to outweigh the loss of frequency resolution, especially at S-band.

4.4 Procedure

In Figure 7 the procedure for deriving the backscattering coefficient is depicted. The different steps indicated in the figure are explained here:
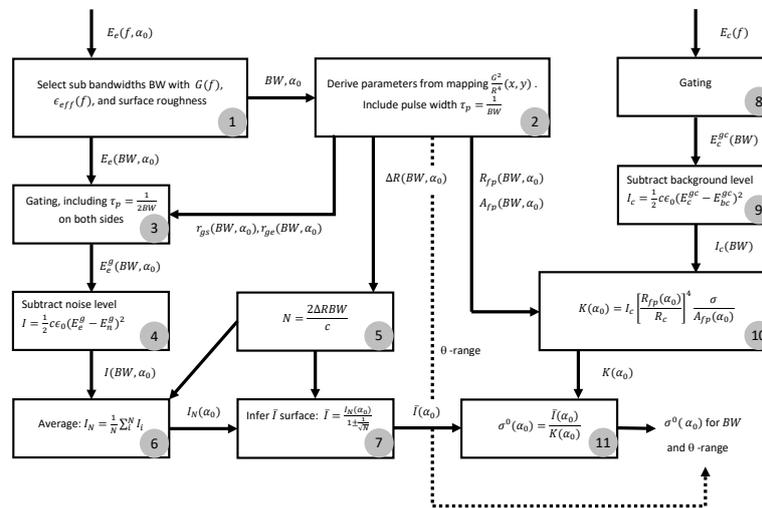
Figure 7. Flowchart of σ^0 derivation process. Inputs are the measured backscattered electric fields of the surface target $E_e(f, \alpha_0)$ and the calibration standard $E_c(f)$. The process follows from 1 to 11 in sequence.

1. We start with E_e measured over the full $0.75 - 10.25$ GHz band at angle α_0: $E_e(f, \alpha_0)$. Bandwidths BW are selected based on the change of $G(\alpha, \beta)$ over frequency (Appendix C), the number of independent frequency samples N that may be retrieved from BW, and the estimated change of backscattering properties over frequency of the ground surface as is discussed in Sec. 4.3. Result is the bandwidth selection $E_e(BW, \alpha_0)$.

2. With BW and α_0 as input, $G^2/R^4(x, y)$ is mapped for all frequencies within BW using the antenna radiation patterns measured by the manufacturer. The region associated with 50 % of the total projected intensity onto the ground is determined to set appropriate gating times, or distances r_{gs}, r_{ge}, and for calculating the A_{fp}, R_{fp}, and the θ range. Half the pulse width $c/(2BW)$ is subtracted from r_{gs} and added to r_{es}, quantities A_{fp}, R_{fp}, and the θ range are changed accordingly.

3. The gate is applied to $E_e(BW, \alpha_0)$, resulting in the gated backscattered field $E_e^g(BW, \alpha_0)$.

4. The noise level signal $E_n^g(BW)$ is subtracted from $E_e^g(BW, \alpha_0)$ for each measured frequency. The result is squared and converted into intensity $I(BW, \alpha_0)$.

5. The number of statistically independent frequency samples N within BW is calculated with $\Delta R = r_{ge} - r_{gs}$ (Sec. 4.3).

6. From the $I(BW, \alpha_0)$ spectrum N intensities are selected at equidistant intervals of $\Delta f = BW/N - 1$ and averaged to $I_N(\alpha_0)$.

7. With $I_N(\alpha_0)$ and N, $\bar{I}(\alpha_0)$ is calculated using Eq. 9. The denominator $1 \pm 1/\sqrt{N}$ implies that $\bar{I}$ is estimated with a 68 % confidence interval.

8. The gated backscattered signal from the reference target $E_c^{gc}(BW)$ is determined for the full $0.75 - 10.25$ GHz band under the assumption that $G \approx 1$ for all frequencies (see Appendix C). After gating the relevant BW of E_c^{gc} is selected.

9. The measured response from the mast without reference target $E_{bc}^{gc}(BW)$ is subtracted from the reference target response. Subscript bc denotes background calibration, the superscript gc indicates that the same gate was used as with the reference target response. The result is squared and converted into intensity $I_c(BW)$.

10. The $I_c(BW)$ is used to calculate the factor K, given the footprint area A_{fp} and centre distance R_{fp} (Eq. 7).

11. The final step is the application of Eq. 6 with $\bar{I}(\alpha_0)$ and $K(\alpha_0)$ as inputs to obtain σ^0. By steps 2 and 6 the derived σ^0 is to be associated with the chosen BW and calculated θ-range. By step 7 a 68 % confidence interval applies to σ^0.

5 Measurement results

5.1 Measurement uncertainty

5.1.1 Fading- and systematic measurement uncertainty

Besides uncertainty due to fading, systematic measurement uncertainty was also considered in the retrieval of σ^0. The radar returns and subsequent σ^0-values derived from it have a systematic measurement uncertainty whose main contributors are the temperature-induced radar return uncertainty ΔE_T^g (Vm^{-1}) and reference target measurement uncertainty ΔK (Vm^{-1}). For both factors we estimate their respective uncertainty levels (see Appendix D1 and Appendix D2 respectively) and how these propagate into an overall σ^0 measurement uncertainty together with the fading uncertainty. In this context we also consider here the system's noise floor E_n^g and the Noise Equivalent σ^0 (NES) derived from it, (see Appendix D3). Table 4 lists all estimated systematic uncertainties and noise floor levels.

Table 4. Summary of systematic uncertainties and noise levels. ΔE_T^g is the temperature-induced radar return uncertainty and ΔK the reference target measurement uncertainty. E_n^g is the noise level and NES the corresponding Noise-Equivalent σ^0.

All values in dB	S-band		C-band		X-band	
	vv	hh	vv	hh	vv	hh
Uncertainties						
ΔE_T^g (absolute error)	-99	-93	-94	-96	$-10 \times 10^{+1}$	$-10 \times 10^{+1}$
ΔK (relative error)	0 – -0.10	0 – -0.16	0 – -0.28	0 – -0.30	0 – -1.2	0 – -1.1
Noise level						
E_n^g (typical value over BW)	-92	-85	-100	-95	$-12 \times 10^{+1}$	$-11 \times 10^{+1}$
NES (typical value over BW)	-37	-30	-40	-36	-48	-42

Starting with Eq. 6 it can be shown (see Appendix D4) that the three estimated types of uncertainty, namely fading, temperature-induces radar return uncertainty (ΔE_T^g), and reference target measurement uncertainty (ΔK) can be combined in a model for total σ^0 uncertainty:

$$\sigma^0 = \frac{I_N \pm \Delta I_N}{(K \pm \frac{2}{3}\Delta K)(1 \pm 1/\sqrt{N})} = \frac{I_N}{K} \pm \Delta \sigma^0 \tag{12}$$

ΔI_N (Wm^{-2}) is a statistical error that follows from ΔE_T^g, ΔK is converted from a maximum possible error into a statistical error with a $(2/3)$ probability confidence interval and the term $1/\sqrt{N}$ represents a statistical error caused by fading. In the right term the three uncertainty contributions are merged into one statistical uncertainty $\Delta\sigma^0$ (m^{2}m^{-2}), which is a 66% confidence interval for σ_0. In this paper these 66% confidence intervals are presented in all figures showing our retrieved σ^0. To give an indication of the magnitude of $\Delta\sigma^0$, which are different per bandwidth, polarization, and overall σ^0-level, some extremes are summarized in Table 5. Shown values were retrieved from the calculated time-series results, which are presented in Section 5.2.3.

Table 5. Example uncertainty values $\Delta\sigma^0$ (dB) per bandwidth, polarization, and overall σ^0-level.

	S-band		C-band		X-band	
	vv	hh	vv	hh	vv	hh
High σ^0-levels (typical in summer)						
	+1.1 – -1.5	+1.2 – -1.7	+1.3 – -1.9	+1.2 – -1.6	+1.1 – -1.5	+1.1 – -1.6
Low σ^0-levels (typical in winter)						
	+1.4 – -2.1	+1.9 – -3.5	+1.8 – -3.2	+1.7 – -2.8	+1.7 – -2.8	+1.7 – -2.8

5.1.2   Uncertainty due to angular resolution antenna patterns

Measuring the dependence of σ^0 on incidence angle θ, $\sigma^0(\theta)$, with a scatterometer whose antenna radiation patterns are $G(\alpha, \beta)$ is equivalent to the convolution of $\sigma^0(\theta)$ with $G(\alpha[\theta], \beta[\theta])$. For a narrow-beamwidth antenna $G(\alpha[\theta], \beta[\theta])$ may be approximated by a block-function whose width is the FWHM beamwidth. This is equivalent to the narrow-beam approximation mentioned in Sec. 4.1, the measured 'convolved' $\sigma^0(\theta)$ is similar to the 'actual' $\sigma^0(\theta)$. With antennas whose FWHM beamwidths probably exceed the rate of change of σ^0 over θ this approximation will lead to larger errors. Still, in principle it is possible to deconvolve the convoluted $\sigma^0(\theta)$ function to obtain the actual $\sigma^0(\theta)$ since $G(\alpha, \beta)$ is known. This deconvolution is performed by Axline (1974) for example, but was considered to be outside the scope of this paper. Instead, the procedure as explained in Sec. 4.1 was followed which, consequently, does result in an unknown uncertainty in the retrieved σ^0.

It is possible, however, to estimate this uncertainty with a simple numerical experiment in which the scatterometer return is simulated using a pre-defined functional type of $\sigma^0(\theta)$. We used the empirical model $\sigma^0_{pq}(\theta)$ for grassland developed by Ulaby and Dobson (1989). When using our retreival method on the simulated scatterometer return we obtain, for 4.75 GHz with vv polarization $\sigma^0_{vv} = -14.4$ dB for $34° \leq \theta \leq 60°$, while the actual value over this interval varies from $-13.0 \leq \sigma^0_{vv} \leq -14.9$ dB. Although this discrepancy depends on the (unknown) form of $\sigma^0(\theta)$, in general this error will be larger for low- and smaller for high frequencies because of the respective antenna beamwidths.

5.2   Measured backscattering coefficients

For the remaining analysis we discuss the results for three bandwidths: $9 - 10$ GHz (X-band), $4.5 - 5.0$ GHz (C-band), and $2.5 - 3.0$ GHz (S-band). These are chosen because their respective wavelengths are doubled with respect to each other: $3.0 - 3.3$ cm, $6.0 - 6.6$ cm, and $10 - 12$ cm.

5.2.1   Angular variation σ^0_{pp} asphalt

We start with the asphalt experiment result, which we present here to demonstrate that our σ^0 retrieval method, using measurement data obtained with our scatterometer system, results in σ^0 -values comparable to those in other studies.

The co-polarization backscattering coefficients over various angles α_0 are shown in Fig. 8. The results are plotted together with curves of the empirical model of $\sigma^0_{pq}(\theta)$ for asphalt described in Ulaby and Dobson (1989). This model was developed by using measurement data of numerous previous studies on asphalt backscattering. For both vv- and hh polarization the measured data shows a clear overall decreasing trend of σ^0 over θ, which is expected from a surface that is smooth compared to the wavelength. Overall, σ^0 for vv polarization is higher than for hh polarization, which is in accordance to the empirical model. Starting from the smaller angles, the consecutive measurement points remain at similar level. With hh polarization there appears to be even a local minimum at $40°$, although the measurement uncertainty is relatively large there. Given that the empirical curves show a similar trend ,though not as pronounced, the slow decay of σ^0_{pp} over θ for $25 - 55°$ can simply be a
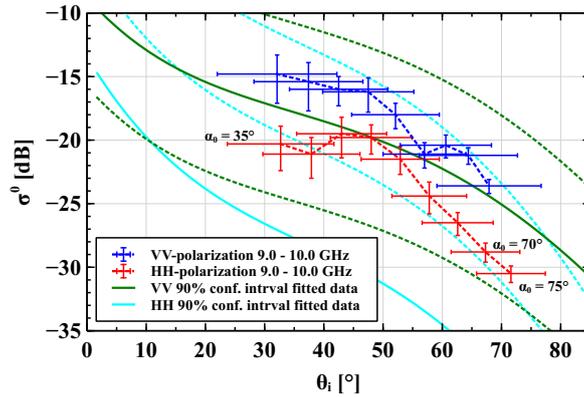
Figure 8. Measurement results of $\sigma^0_{pp}(\alpha_0)$ for asphalt within 9 - 10 GHz band vs. Ulbay's empirical model 1989. Points represent measurement results for different antenna boresight angles α_0. Horizontal bars represent intervals for angle of incidence θ and vertical bars the 66% confidence interval for σ^0. Dotted lines between data points are guide to the eye. Solid and dotted curves (green and cyan) represent mean value and 90% confidence interval of empirical model respectively.

property of asphalt. Overall we find our measurements to lie within the 90 % occurrence interval of the empirical model and, therefore, conclude that our results for asphalt are similar to the experiments used by Ulaby and Dobson (1989).

410 5.2.2 Angular variation σ^0_{pp} Maqu

With the scatterometer experiments where the radar return of the Maqu-site surface was measured at various antenna boresight- (α_0) and azimuth (ϕ) angles we intent to achieve the following. First, to quantify the behaviour of σ^0 with respect to the elevation angle (θ), BW, and polarization for the Maqu site ground surface with a living vegetation canopy. Second, to asses the spatial homogeneity of $\sigma^0(\theta)$ over the Maqu-site surface. As explained in Sec. 4.3, the single footprint area for the σ^0
415 time-series measurements should be representative for the whole Maqu-site surface.

Due to practical limitations of possible ϕ angles and because of the wide antenna beam widths, the footprints of used α_0- and ϕ combinations in this experiment overlap partially, as is shown in Fig. 2) However, since we employ frequency averaging to reduce the fading uncertainty for every footprint, we argue that the σ^0 -values retrieved per (overlapping) footprint may be
420 compared to each other for this section's analysis.
Figures 9 and 10 show measured backscattering coefficients for different α_0- and ϕ angles for X- and for S-band respectively. There is a clear tendency of σ_0 decreases with α_0. Deviations from this trend, for example with X-band at $\phi = 10°$, $\alpha_0 = 50°$, might point to local strong scattering, but could also simply be due to fading. Since the S-band response for the same ϕ shows

a clear decreasing trend of σ_0 over α_0 it is probably the latter.

425
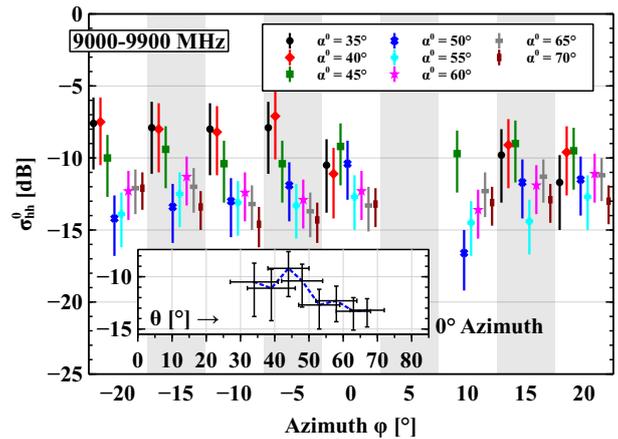
Figure 9. Measurement of $\sigma_{hh}^0(\alpha_0, \phi)$ for 9.0 - 9.9 GHz sub band over Maqu site on 20170825. Main figure: For different antenna boresight azimuth angles ϕ σ_{hh}^0 over boresight elevation angles α_0 is shown. The 8 vertical bars represent the 66% confidence interval for σ^0. Intervals for incidence angles θ per measurement are not shown here for clarity of figure. Inset: $\sigma_{hh}^0(\alpha_0)$ for $\phi = 0°$. Horizontal bars represent intervals of actual incidence angles θ.
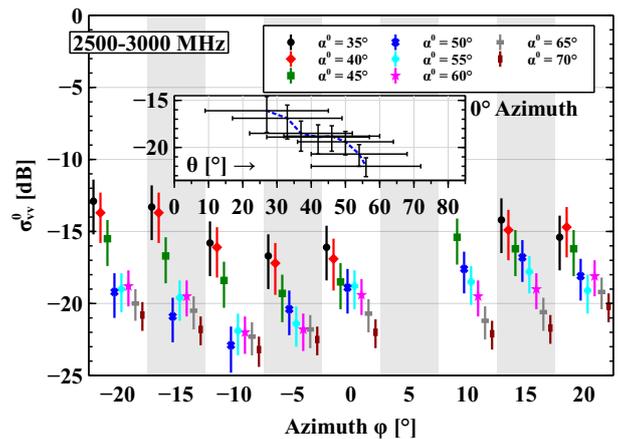
Figure 10. Measurement of $\sigma_{vv}^0(\alpha_0, \phi)$ for 2.5 - 3.0 GHz sub band over Maqu site on 20170825.

As a means to quantitatively evaluate the σ^0 behaviour with respect to θ- and ϕ angle the data is grouped in sets of σ^0 over α_0 for every angle ϕ, BW, and polarization. Next, an iterative least-squares non-linear fitting algorithm is applied to fit each set to the model

$$\sigma^0 = A \cos(\theta)^B \tag{13}$$

430 where A is a constant $(\mathrm{m}^2\mathrm{m}^{-2})$ and B is either 1 for an isotropic scatterer or 2 for a surface in accordance with Lambert's law (Clapp, 1946). Since the retrieved σ^0 values are in fact 66% confidence interval for σ^0, we used the centre σ^0 -values for the fitting process. Figure 11 shows the A coefficients found for both values of B. As a next step, we reduced the number of possibilities by selecting for each polarization-BW combination the most likely value for B (1 or 2). This was done by tallying over the ϕ -angles which of the two fitted curves $\sigma^0 = Acos(\theta)^B$ passed through the confidence intervals best and had the

435 highest coefficients of determination (R^2) (numbers in Fig. 11). The outcome was $B = 1$ for X-band vv- & hh polarization, C-band hh polarization and $B = 2$ for C-band vv polarization and S-band vv- & hh polarization as indicated by the arrows in Fig 11. Finally, with the found parameters A and B we assess the behaviour of $\sigma^0(\theta)$ for the different angles ϕ, BW, and polarizations.

We comment first on the found B coefficients which characterize the angular dependence $\sigma^0(\theta)$. The stronger decrease over
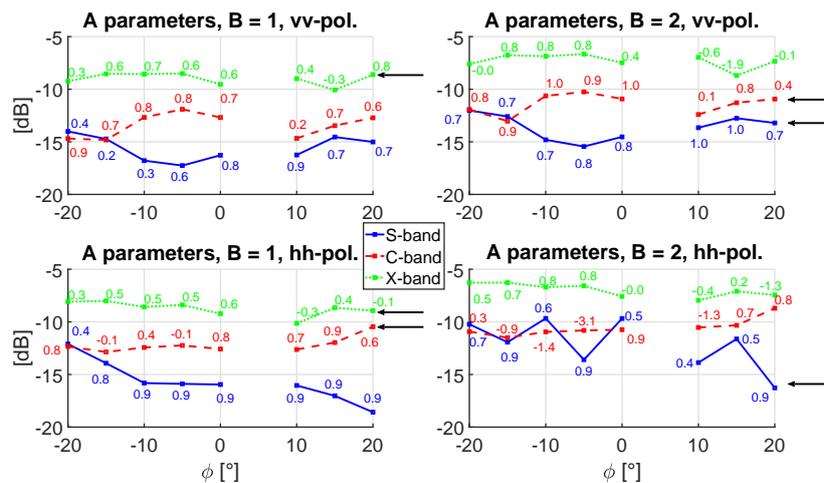
Figure 11. Results of fitting $\sigma_{pp}^0(\alpha_0)$ to model $\sigma_0(\theta) = Acos(\theta)^B$ for different azimuth angles ϕ, frequency sub bands, and polarizations. Vertical axes show found values for A. Numbers at data points represent values for coefficient of determination $(R^2.)$

440 angle found with S- and C-band $(B = 2)$ is as expected since for longer wavelengths the soil surface appears more smooth compared to the surface's roughness. It is well known, see for example (de Roo and Ulaby, 1994), that the more smooth a surface is the more its specular reflection approaches the angular behaviour of the Fresnel model for optics, leading to less scattering in the non-specular directions including the backward direction. Also, for longer wavelengths there is little volume backscattering from vegetation. By the same logic for X-band (shorter wavelengths), σ^0 will decrease more slowly over θ

445 and also the vegetation volume scattering is stronger, hence $B = 1$, the model for an isotropic scattering surface applies. The reported behaviour of $\sigma^0(\theta)$ in conjunction with wavelength is in accordance with results of Stiles et al. (2000) for a short green wheat canopy.

Next we focus on the found magnitudes of A, which is basically the backscattering coefficient σ^0 given a fixed θ. For both vv- and hh polarization, X-band has the highest A values for all ϕ angles. With vv polarization A decreases with increasing

450   wavelength, except for $\phi = -20$ and $-15°$ where values for C- and S-band are similar. This behaviour was expected, again because of a surface appearing more rough, and the radiation-vegetation interaction (or scattering) being stronger for shorter wavelengths. However, with hh-polarization A for S-band appeared larger than, or equal to, that for C-band at positive ϕ - angles. What also stands out is the large variation of A over ϕ for S-band. We do not have an explanation for this behaviour with hh polarization.

455   Finally some remarks on the variation of A with ϕ and, virtually, arccos the surface area. Except for X-band with hh polarizations there did not appear to be a systematic trend of A over ϕ. Also, there was not one particular ϕ angle for which the values for A over BW and polarization stood out from the rest. These observations indicate that the surface area covered by our scatterometer appeared to have uniform (scattering) properties. The somewhat higher A values with the negative ϕ values with X-band at hh polarization are probably caused by a difference in vegetation density between the left- and right side of

460   the Maqu site. Fortunately, for $\phi = 0°$ the A value had a medium value compared to the other ϕ angles, so that we may still interpret the surface area associated with the scatterometer's (fixed) footprint during the time-series measurements as being representative for its surroundings.

5.2.3   Time-series σ^0_{pp} Maqu

465   Figure 12 presents an overview of the time-series data of σ^0_{pp} over the whole August 2017 – 2018 period for all considered bandwidths in S-, C-, and X-band, along with m_v and T_{soil} at 2.5 and 5 cm depth. For visibility reasons the graphs only display measurements taken at 18:10 with 2 day intervals. Data of the radar return and σ^0_{pp} for November 2017 is not available, while that of late June – Early July 2018 will become available at a later stage.

We observe for all bands and polarizations that σ^0 is highest in summer and autumn while being lowest during winter. This

470   may be explained by the fact that in summer and autumn m_v, and the amount of fresh biomass is high. As a result, the high dielectric constant of moist soil, in combination with the rough surface and presence of water in the vegetation results in strong backscattering. During winter, however, there is little liquid water, i.e. m_v, present in the soil and no fresh biomass (dry biomass however remains present). The dielectric constant of the soil therefore is lower compared to that of moist soil and there is little to no scattering from the dried out vegetation, resulting in a lower σ^0_{pp}. There were however peaks of σ^0_{pp} during winter, for

475   example on 26 January, which coincided with snowfall. Snow cover, deposited on the layer of dead vegetation, forms a rough surface that allows for strong backscatter. The dynamics of σ^0_{pp} during thawing period will be discussed in more detail below. When comparing the three bands we observe that, in general, the backscattering is highest at X-band and lowest at S-band. This difference is caused by the wavelength-dependent response to the surface roughness of the soil and vegetation during the summer and autumn period. For longer wavelengths the soil surface 'appears' more smooth than for the shorter wavelengths,

480   resulting in stronger specular reflection, thus lower backscatter. A similar argument holds for the vegetation; its constituents are small compared to the longer wavelengths, thus little volume scattering occurs.

Except for during the summer, backscatter for vv polarization was equal to, or higher than that of hh polarization. This behaviour was also observed by Oh et al. (1992), albeit for bare soil. We however may compare our situation to that of bare
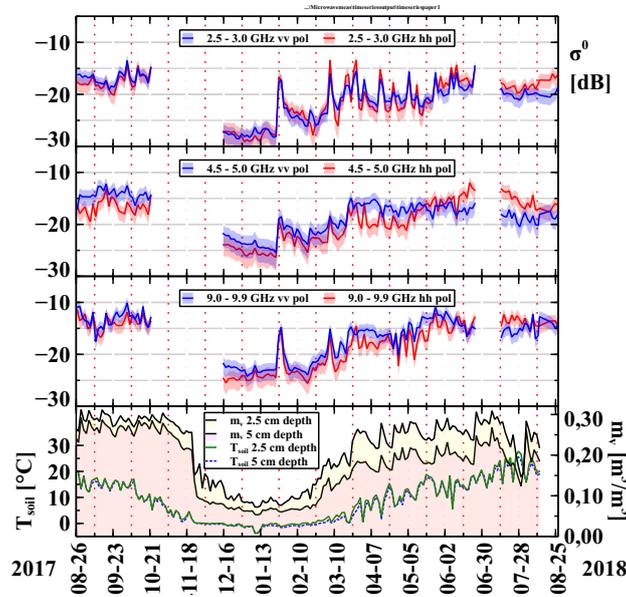
Figure 12. Time-series measurements of σ^0 (m^{2}m^{-2}) for vv and hh polarizations for S-, C- and X-band from August 2017 to 2018. Shown are measurements taken at 18:10 with 2 day intervals. Shaded regions indicate 66% confidence intervals for σ^0. Antenna boresight angle fixed at $\alpha_0 = 55°$. Range angles of incidence are: S-band; $32° \leq \theta \leq 60°$ for vv- and $20° \leq \theta \leq 60°$ for hh, C-band; $34° \leq \theta \leq 60°$ for vv- and $39° \leq \theta \leq 61°$ for hh, X-band; $47° \leq \theta \leq 59°$ for vv- and hh. Bottom graphs show measured volumetric soil moisture content m_v^{5TM} (m^{3}m^{-3}) and soil temperature T_{soil} at 2.5 and 5 cm depth. Spatial average volumetric soil moisture content M_v is estimated as $M_v = m_v^{5TM} \pm 0.04$ m^{3}m^{-3}. Black arrows indicate rain events, specified by two numbers: rate (mmh^{-1}) $\times$ duration (h).

soil during winter, when there is no fresh biomass. When vegetation was present, σ_{hh}^0 was stronger, as is visible during July
- August 2018. This was however not the case during August - September 2017, when the vegetation probably still contained water. Somewhat stronger backscatter, $0.5 - 1$ dB, for hh- than for vv polarization was also reported for grassland in Ulaby and Dobson (1989) with $40 \leq \theta \leq 60°$ for S- and X-band. For C-band they reported no clear difference. Yet another study, (Kim et al., 2014), measured 3-4 dB higher backscatter for hh as for vv for wheat at L-band ($\theta = 40°$).

Figure 13 shows a 13-day period with σ_{pp}^0 measured during soil freeze/thaw transitions at 30 minute intervals. In the bottom graph we observe that measurements taken with 5TM sensors at 2.5 and 5 cm depth. T_{soil} was above 0 °C during daytime and just below it for some nights. With some days m_v showed diurnal thawing and freezing. The arrows indicate two rain events, with the first it rained 1 mmh^{-1} for 2 hours and with the second 1 mmh^{-1} for 10 hours.

The most prominent features in the backscatter measurements are the diurnal variations of σ_{pp}^0 that are clearly caused by changes of m^v. For all bands and polarizations we observe that σ^0 increases during daytime due to the increase of liquid water in the top soil due to thawing and at night σ^0 drops as most of the water freezes again. With some days, e.g. 3 to 5 April, we observed diurnal changes in σ^0 while the m_v measured by the 5TM sensors showed little variations. This may suggest that the freezing and thawing during those days occurred only in the very top-soil layer, just below the air-soil interface where it was
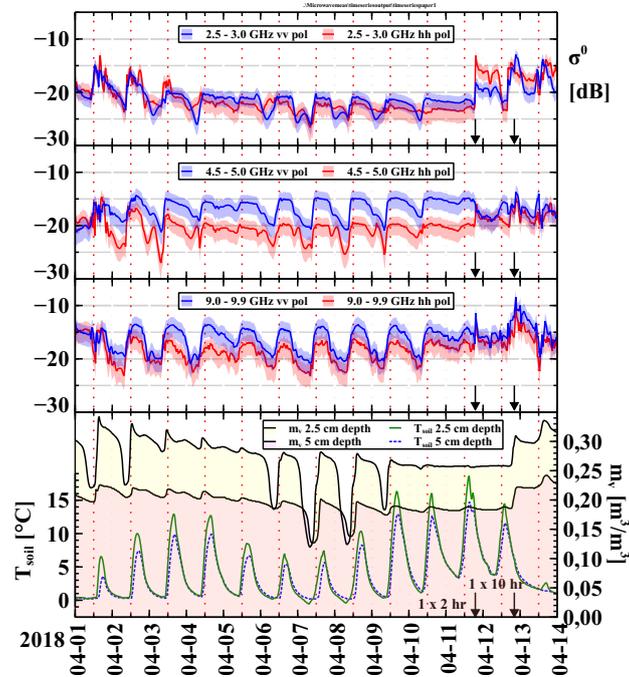
Figure 13. Time-series measurements of σ^0 (m^{2}m^{-2}) for vv and hh polarizations for S-, C- and X-band during 13 days in April 2018. Shaded regions indicate 66% confidence intervals for σ^0. Antenna boresight angle fixed at $\alpha_0 = 55°$. Range angles of incidence are: S-band; $32° \leq \theta \leq 60°$ for vv- and $20° \leq \theta \leq 60°$ for hh, C-band; $34° \leq \theta \leq 60°$ for vv- and $39° \leq \theta \leq 61°$ for hh, X-band; $47° \leq \theta \leq 59°$ for vv- and hh. Bottom graphs show measured volumetric soil moisture content m_v^{5TM} (m^{3}m^{-3}) and soil temperature T_{soil} at 2.5 and 5 cm depth. Spatial average volumetric soil moisture content M_v is estimated as $M_v = m_v^{5TM} \pm 0.04$ m^{3}m^{-3}. Black arrows indicate rain events, specified by two numbers: rate (mmh^{-1}) $\times$ duration (h).

outside the influence zone of the 5TM sensors. The time lag between the drop of σ^0 (first) and the drop of 5TM m_v (second), is caused by the same phenomena as the freezing starts at the top soil layer and progresses downward. The time lag during thawing was smaller.

In general the magnitude of the σ^0 -change was largest for X-band and smallest for S-band. This can be explained by the penetration depth. Longer wavelengths penetrate deeper into the soil. As such, should there be radiation scattered back from below the surface then it will have travelled deeper into the soil for S-band than for X-band. As such, the response for X-band will be sensitive to changes in m_v only at the top soil level, while for S-band signatures of change at the top soil layer will be affected by contributions from the deeper layers, in which m_v changes less over time.

Although there are many more interesting features visible only from Fig. 13 alone, a more detailed investigation of the results extend beyond the scope of this paper. Our preliminary analysis demonstrates that the scatterometer data set collected at fixed time-intervals over a full year at the Maqu site contains valuable information on exchange of water and energy at the land-

510 atmosphere interface. Information which is difficult to quantify with in-situ measurements techniques alone. Hence further investigation of this scatterometer data set provides an opportunity to gain new insights in hydro-meteorological processes, such as freezing and thawing, and how these can be monitored with multi-frequency scatterometer observations.

6 Data Availability

In the DANS repository, under the link https://doi.org/10.17026/dans-zc5-skyg the collected scatterometer data is publicly
515 available (Hofste and Su, 2020). Stored are both the radar-return amplitude and phase for all four linear polarization combinations and processed σ^0 for co-polarization channels (vv & hh). The dataset includes time-series measurements from 26 August 2017 – 26 August 2018, data of angular variation experiment, and radar returns of the reference targets. Accompanying data includes time-series measurements of soil moisture and -temperature profile at depths of [2.5, 5.0, 7.5, 10, ...90, 100 cm] and precipitation measurements.

520

7 Conclusions

In this paper we describe a microwave scatterometer system that was installed on an Alpine Meadow over the Tibetan Plateau and its collected dataset consisting of measured radar returns from the ground surface. The observation period was August 2017 – August 2018 and measurements were taken with a one- to half hour temporal resolution. The scatterometer measured
525 the radar return amplitude and -phase over a 1 – 10 GHz band for all four linear polarization combinations. The system was build with commercially available components (vector network analyzer, four phase stable coaxial cables, and two broadband dual polarization gain horn antennas) and required little to no maintenance.

We described a procedure on how to retrieve the co-polarized backscattering coefficients σ^0_{vv} & σ^0_{hh} for a VNA-based scat-
530 terometer system with two fixed antennas operating over a broad frequency range (1 – 10 GHz). The typical effects resulting from the wide antenna radiation patterns were dealt with by using the narrow-beam approximation in combination with the mapping of function $G^2/R^4(x,y)$ over the ground surface, so that proper footprint positions and -areas, and incidence angle ranges could be derived. The incidence angle range was frequency-dependent and varied from $20 - 65°$ for L-band to $47 - 59°$ for X-band. Since spatial averaging was not possible frequency averaging was applied to reduce fading uncertainty. Bandwidths
535 for averaging were selected with help of the Improved Integral Equation Model (I^{2}EM) for surface scattering.

Backscatter measurements on a rectangular metal plate reference target were used to calibrate the scatterometer. Verification measurements on the co-polarized radar cross section of a metal dihedral plate showed the calibration to be valid. Measurements of the angle-dependent σ^0_{vv} & σ^0_{hh} of asphalt agreed with previous findings, thus showing our σ^0 retrieval method to be
540 accurate.

The uncertainty of our retrieved σ^0 can be divided in a known part estimated from fading- and systematic measurement uncertainty, and an unknown part due to low angular resolution of the used antennas. The known measurement uncertainty in σ^0 was estimated with an error model providing 66 % confidence intervals that are different over frequency bands, polarizations and the overall level of the radar return. Extreme values for $\Delta\sigma^0$ were $\pm$ 1.3 dB for X-band with vv polarization when the overall

545   σ^0 level was highest (during summer) and $\pm$ 2.7 dB with hh polarization when the overall σ^0 level was lowest (during winter). Despite aforementioned uncertainty in σ^0 and the additional unknown uncertainty, we believe that the strength of our approach lies in the capability of measuring σ^0 dynamics over a broad frequency range, $1-10$ GHz, with high temporal resolution over a full-year period.

On three days during summer the radar backscatter was measured for different angles in elevation and azimuth to quantify

550   the angular dependence of σ^0 and to assess the ground surface homogeneity. Presented analysis on the angle-variation data of σ^0 showed wavelength- and polarization dependent scattering behaviour due to vegetation that is in accordance with theory and previous findings. Furthermore, these measurements indicated that the surface associated with the (fixed) footprint for the time-series measurements to be representative of its surroundings.

555   In the retrieved time-series of σ^0_{vv} & σ^0_{hh} for S-band ($2.5-3.0$ GHz), C-band ($4.5-5.0$ GHz), and X-band ($9.0-10.0$ GHz) we observed characteristic changes or features that can be attributed to seasonal changes in the soil. For example a fully frozen top soil, freeze-thaw changes in the top soil, emerging vegetation in spring, and drying of soil.

Further studies with obtained dataset allows for in-depth analysis of diurnal changes of surface top-soil moisture dynamics during all periods within the year. Availability of backscattering data for multiple frequency bands allows for studying scatter-

560   ing effects at different depths within the soil and vegetation canopy during the spring and summer periods. Finally, combining scatterometer data with measured ELBARA-III radiometry data (Su et al., 2020) creates a complementary dataset that allows for in-depth study of the soil moisture and -temperature dynamics below, and at, the air-soil interface.

Author contributions. JH wrote this paper, installed and operated the scatterometer system, developed the data processing, σ^0 retrieval

565   process, and performed the data analysis. RvdV advised in the experiment designs, σ^0 retrieval process and paper structure. XW, ZW and DZ, handled the China customs logistics, installed and operated the scatterometer system. On a regular basis they maintained the scatterometer system and the Maqu site. CvdT advised in the σ^0 retrieval process. JW and ZS conceptualized the experiment design. All co-authors commented and revised the paper.

Competing interests. All authors declare that there are no conflicts of interests

570 *Acknowledgements.* The authors would like to express their gratitude towards the European Space Agency (ESA) and Ministry of Science and Technology (MOST) of the P.R. China for funding this research as part of the Dragon 4 cooperation programme.

List of Symbols

A_{fp}	Surface area of the footprint.	m^2
a	a dimension of reference target frontal projection.	m
α	Angle between tower's vertical axis and the orthogonal projection of the line from antennas to a ground surface segment onto the plane formed by the tower's vertical axis and the antenna boresight direction line. See also Fig. 4. For antenna boresight line $\alpha = \alpha_0$.	°
BW	Bandwidth associated with E_e or σ^0.	GHz
b	b dimension of reference target frontal projection.	m
β	Angle between line from antennas to a ground surface segment and projection of that same line onto the plane formed by the tower's vertical axis and the antenna boresight direction line. See also Fig. 4. For antenna boresight line $\beta = \beta_0$.	°
c	Speed of light.	ms^{-1}
D	Antenna aperture width.	m
ΔE_T^g	Temperature-induced radar return uncertainty.	Vm^{-1}
ΔI_N	Uncertainty in I_N.	Wm^{-2}
ΔK	Reference target measurement uncertainty.	Wm^{-2}
E_e	Magnitude of total electric field strength at the receive antenna, originating from the (surface) target.	Vm^{-1}
E_e^g	Same as E_e, superscript g denotes Time-domain filter, or gate, is applied.	Vm^{-1}
E_n^g	Noise level of E_e. Superscript g denotes that same time-domain filter, or gate, as used with E_e^g is applied.	Vm^{-1}
E_c^{gc}	Magnitude of total electric field strength at the receive antenna, originating from the reference target. Superscript gc denotes Time-domain filter, or gate, is applied.	Vm^{-1}
E_{bc}^{gc}	Background level of E_c^{gc}.	Vm^{-1}
ϵ_0	Permittivity of vacuum (and by approximation that of air).	CV^{-1}m^{-1}
ϵ_{soil}	Effective relative permittivity of a soil, which is a mixture of dry soil, water, minerals, organic material etc. Includes both real and imaginary part component.	−
G	Antenna gain as a function of angle with respect to antenna boresight direction. Maximum value is G_0.	−
H_{ant}	Height of the antenna apertures above the ground.	m
I	Time-average intensity of total electric field strength at receive antenna, originating from the (surface) target.	Wm^{-2}
I_N	Measured intensity averaged over N independent samples.	Wm^{-2}
$\bar{I}$	The average of a large amount of independent measurements of I originating from a surface with backscattering coefficient σ^0. $\bar{I}$ is a surface property.	Wm^{-2}
K	Constant (over BW) linking σ^0 to $\bar{I}$	Wm^{-2}

L	Maximum dimension of target in context of RCS measurement.	m
M_v	Spatial average volumetric top soil moisture content over Maqu site.	$\mathrm{m^3 m^{-3}}$
m_v	Volumetric soil moisture content.	$\mathrm{m^3 m^{-3}}$
N	Number of independent scatterometer measurements, or samples, of a (surface)	$-$
NES	Noise Equivalent σ^0.	$\mathrm{m^2 m^{-2}}$
P_q^{RX}	Power received by radar or scatterometer. The subscript refers to the linear polarization direction (horizontal h or vertical v) that is measured by the antenna.	W
P_p^{TX}	Power transmitted by radar or scatterometer. The subscript refers to the linear polarization direction (horizontal h or vertical v) that is transmitted by the antenna.	W
P_q^c	Power received by radar or scatterometer from calibration target. The subscript refers to the linear polarization direction (horizontal h or vertical v) that is measured by the antenna.	W
ϕ	Azimuth, or horizontal rotation angle of antennas.	°
R	Distance antennas to (area) target (segment).	m
R_c	Distance antennas to calibration standard.	m
R_{ff}	Distance from antennas beyond which the antenna far-field radiation region is defined.	m
R_{fp}	Distance antennas to centre of footprint.	m
R_{pw}	Distance from antennas beyond which the wavefront of transmitted radiation is considered planar.	m
r_{sg}	Start of the time-domain filter, also known as gate.	m
r_{eg}	End of the time-domain filter, also known as gate.	m
σ_{pq}	Radar Cross Section (RCS). The first subscript is the polarization direction (horizontal h or vertical v) of the incident radiation and the second subscript that of the scattered radiation.	$\mathrm{m^2}$
σ_{pq}^0	Backscattering coefficient. The first subscript is the polarization direction (horizontal h or vertical v) of the incident radiation and the second subscript that of the scattered radiation.	$(-)$
T_{soil}	Soil temperature.	°C
T_{encl}	Temperature inside VNA enclosure.	°C
τ_g	Temporal width of the time-domain filter, also known as gate	s
τ_p	Temporal pulse width.	s
W_{ant}	Separation distance between the two antenna apertures.	m
w_g	Spatial width of the time-domain filter, also known as gate.	m

Appendix A: Derivation spatial soil-moisture-variation estimate

At every depth, m_v varies over the horizontal spatial extent at all scales (Famiglietti et al., 2008). Local m_v variability is caused by variations in soil structure and texture, including organic matter. At the Maqu site, the 5TM sensor array forms only one spatial measurement point for soil moisture. We denote its measurements as m_v^{5TM} ($\mathrm{m^3 m^{-3}}$). In an attempt to quantify how m_v^{5TM} at the top soil layer (depths 2.5 and 5 cm) relates to the soil moisture over the rest of the Maqu site, we sampled m_v at 17 positions along the no-step zone (Fig. 2) on June 29th 2018 with a hand held impedance probe, type ThetaProbe ML2x, whereby 3 measurements were taken per position. Figure A1 shows the measured m_v in the top layer. Taking aside the outlying
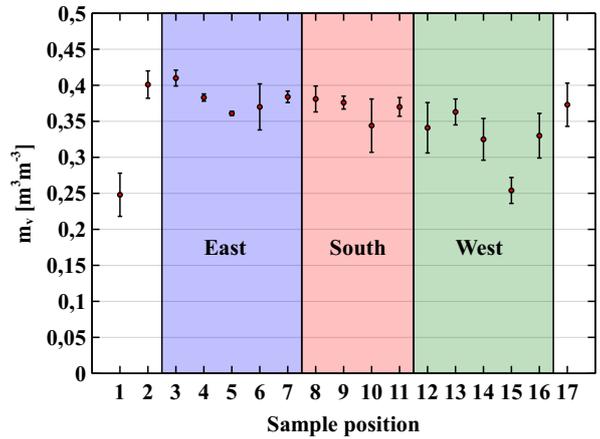
Figure A1. Top-soil m_v measured with hand-held ThetaProbe at 17 sample positions along no-step zone periphery (indicated Fig. 2). Vertical bars denote minimum and maximum values of the 3 measurements per sample position. Red dots represent median values.

values at positions 1 and 15, we observe that the trend along the periphery is slightly larger than the variability amongst the three measurements taken at a specific position. The average standard deviation over the 15 positions is 0.03 $\mathrm{m^3 m^{-3}}$ while the average standard deviation over the three measurements is 0.02 $\mathrm{m^3 m^{-3}}$. Given this small difference we concluded there is no clear trend of top soil m_v at the Maqu site. Therefore, we considered all $15 \times 3 = 45$ readings as independent measurements on spatial m_v variation, that we used to create the quantity S_t ($\mathrm{m^3 m^{-3}}$), called the total standard deviation of spatially measured m_v, which is an estimate for the spatial m_v variability over the Maqu site. Subsequently, we use S_t to relate the measured m_v^{5TM} to the spatial average top soil moisture content over the Maqu site M_v ($\mathrm{m^3 m^{-3}}$) according to

$$M_v = m_v^{5TM} \pm S_{tot} \tag{A1}$$

Using the assumption of temporal stability of spatial heterogeneity (Vachaud et al., 1985) we consider found S_t to hold throughout the year. S_t. is calculated by

$$S_t = \sqrt{S_s^2 + S_{5TM}^2 + S_p^2} \tag{A2}$$

The term S_s ($\mathrm{m^3m^{-3}}$) represents the spatial m_v variability as measured along the periphery. It is calculated as the standard deviation over $45 - 1$ samples and is 0.031 $\mathrm{m^3m^{-3}}$. The standard deviation S_{5TM} a has value of 0.02 ($\mathrm{m^3m^{-3}}$) and is the

595 root-mean-square measurement error of the 5TM sensors. It was derived in Zheng et al. (2017b) after calibrating 5TM sensor retrievals to top-soil gravimetric soil samples taken at the Maqu site. The term S_p is the propagated error of the 0.05 $\mathrm{m^3m^{-3}}$ theta probe measurement accuracy (Table 2) when S_s is calculated. $S_p = 0.05/\sqrt{45 - 1} = 0.0075$ $\mathrm{m^3m^{-3}}$. Finally, S_t then is 0.04 $\mathrm{m^3m^{-3}}$.

Appendix B: Details scatterometer calibration

600 ### B1 Measurement of reference targets

We measured the radar returns of reference targets with known radar cross section (RCS) σ_{pq} in order to calibrate the scatterometer. A rectangular metal plate was used as reference target for the co-polarization channels. Next, as verification of the calibration process we measured σ_{pp} of a metal dihedral reflector. The physical optics model used for calculating the RCS of a metal plate and dihedral reflector is

605 $$\sigma_{pp} = 4\pi \frac{(ab)^2}{\lambda^2} \tag{B1}$$

where a and b are the standards' dimensions (m) in the frontal projection (Kerr, 1951). There are validity conditions for model B1 which concern the reference target's size and the distance at which it is measured R_c. Additionally, R_c should be picked such to prevent interferences from ground reflections. Table B1 lists the used R_c values for the deployed reference standards. We first describe the validity conditions for model B1.

Conditions for Eq. (B1) are that the standard's largest dimension L (m) is large compared to the wavelength, i.e. $L > \lambda$, and

Table B1. Deployed reference standards and their bandwidths of validity

	Distance R_c :	PW -criteria met for:	$L/\lambda \geq 3$ for:
Large rectangular plate, a = 85 cm, b = 65 cm	36.3 m	$f \leq 7.5$ GHz	$f \geq 1.5$ GHz
Small dihedral reflector, a = 57 cm, b = 38 cm	27.7 m	$f \leq 13$ GHz	$f \geq 2.4$ GHz
Large dihedral reflector, a = 120 cm, b = 65 cm	27.7 m	$f \leq 3$ GHz	$f \geq 1.4$ GHz

610

that the incident wavefront is close to planar. Kouyoumjian and Peters (1965) proposed the following equation for calculating the minimum distance R_{pw} (m) beyond which the wavefront can be considered planar (allowing for a $\pi/8$ phase error):

$$R_{pw} = \frac{2L^2}{\lambda} \tag{B2}$$

Concerning the condition $L > \lambda$, previous measurements (Hofste et al., 2018) showed, empirically, that for $L/\lambda \geq 3$ model

615 (B1) matches a standard's measured σ_{pp} within 1 dB. Besides used R_c values, Table B1 also lists the frequency ranges for which the plane wave criteria (using the stated values R_c) and the size criteria hold. The plane-wave criteria with the rectangular plate

was not met for 7.5 - 10 GHz. Yet the verification measurement of σ_{pp} for the small dihedral reflector (see Sec. B2) showed satisfactorily resemblance with the model B1 values, indicating that the calibration (using the large rectangular plate) was correct for 7.5 – 10 GHz.

620 Now we describe the ground interference issue. Figure 4(b) depicts two pathways for the scatterometer signal to travel to the calibration standard and back. We wish to only measure the response travelling via the direct pathway, $2 \times R_c$. Any contributions from alternative pathways that travel via ground reflections, as shown in the figure, are undesirable since these could interfere with the direct path response. Undesired ground reflections can be removed during post-processing via time-domain filtering, or gating (see Sec. 3.2 and Appendix C), provided the difference in total travel time, or distance, is large enough. Naturally,

625 with greater R_c the difference $R_c - (R_1 + R_2)$ will become smaller. We used a minimum distance of 1.1 m, which follows from the sum of the used gate width for the calibration target $\tau_g = 1.7$ ns, which is equivalent to $w_g = 0.5$ m plus the widest used pulsewidth resulting from the narrowest used frequency bandwidth BW of 0.5 GHz (Sec. 4.3): $\tau_p = 1/BW = 2$ ns, which is equivalent to $c\tau_p = 0.6$ m. The ground reflection shown in Fig. 4(b) was the pathway whose distance was closest to that of the direct route. Since the difference between $2R_c$ and $R_1 + R_2 + R_c$ was 1.35 m (< 1.1 m) we were able to filter this out. The

630 metal fence of the Maqu site posed another potential source of interference, but because it was separated from the calibration standards by at least 4 m its contribution was easily filtered out with the employed gating filter.

B2 Results calibration validation

Figure B1 shows the measured radar returns $E_c^{gc}(f)$ of the three calibration standards, whose shapes over frequency are explained as follows. With all returns there is a sharp trough between 8 – 9 GHz, which is caused by a combination of a local

635 increment of the antenna's return loss and an asymmetry in the antennas E-plane radiation pattern between 7 – 9 GHz. The asymmetry causes the pattern's peak to point off-target by about $10°$ resulting in a lower radar return. The deep troughs close to 1.3 GHz are caused by a combination of high return loss at the low-frequency edge of the antenna's operational bandwidth and an artefact of the gating procedure, which in this case lets $E_c^{gc}(f)$ rise at the edge. This gating artefact is known to distort the band edges of a gated frequency response (Agilent, 2012). To account for this artefact the bandwidths used for the ground

640 surface measurements were broadened by 10% at both edges prior to gating. The added edges were discarded again after gating. The curves of the rectangular plate and small dihedral reflector have a similar shape for most of the frequency band. Their difference is merely a constant factor as predicted by the physical optics model for RCS (Eq. B1). The curve shape of the large dihedral reflector however is clearly different from the other two because the planar-wave condition, necessary for model B1, is not met for most of the frequency band, see Table B1.

645

The radar return of the large rectangular plate was used to calibrate the scatterometer for co-polarization. To validate the calibration we derived the RCS of both dihedral reflectors. As is shown in Fig. B2, the RCS of the small dihedral reflector matches the physical optics model satisfactorily from 4 – 10 GHz. The local peak between 8 – 9 GHz is caused by aforementioned radiation pattern asymmetry that causes any minor misalignments between the two standards, i.e. antennas with respect

650 to the rectangular plate vs. antennas with respect to dihedral reflector, to result in erroneous RCS values. Furthermore, with
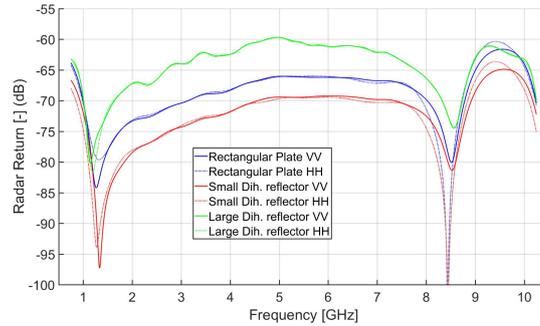
Figure B1. Measured radar returns of calibration standards for co polarization E_c^{gc}. Solid lines are VV- and dotted lines are HH polarization.
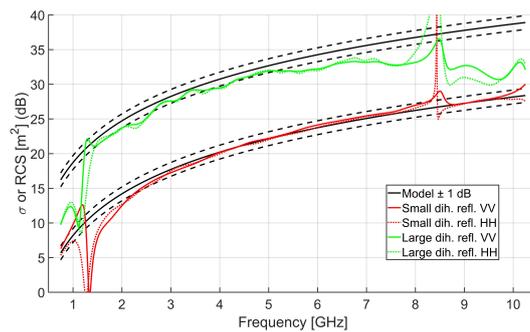
Figure B2. Measured RCS values of small and large dihedral reflectors as verification of Co-pol scatterometer calibration. Red curves are RCS of small dihedral reflector, green curves that of large dihedral reflector. Solid lines are VV- and dotted lines HH polarization. Solid black lines represent theoretical physical optics model of the RCS. The dotted lines above and below are 1 dB deviation lines shown here as guide to the eye.

hh polarization the rectangular-plate return (Fig. B1) was close to noise level at 8.4 GHz resulting in division by a very small number when calculating the RCS. Below 2.5 GHz the retrieved RCS starts deviating from the theoretical curve because the standard's dimensions become too small compared to the wavelength. Note that 2.5 GHz is close to the value listed in Table B1 based on the empirical requirement $L/\lambda \geq 3$. The measured RCS of the large dihedral reflector is lower than the theoretical curve above 4 GHz because its distance R_c is too small to satisfy the planar-wave condition. Between $1.5 - 3$ GHz the retrieved RCS is still about 1 dB lower compared to that of the model value. However, the measured curve's slope matches that of the theoretical curve satisfactorily, better in fact than that of the small dihedral reflector over the same frequency range. The reason being that the criteria $L > \lambda$ is clearly met for the large dihedral reflector.

We conclude that by using the rectangular plate as reference target for calibrating the scatterometer, measured σ_{pp}^0 values are accurate between $1.5 - 10$ GHz with an offset of approximately -1 dB for $1.5 - 3$ GHz.

Appendix C: Gating

For simplicity, instead of using the (complex) electric field strength measured at the scatterometer's receive antenna E_e, we explain the gating process with the term X (V), which can be considered proportional to E_e by some scatterometer system constant. The measured frequency-domain signal $X[\omega_h]$ was transformed into the time-domain via the Inverse Digital Fourier Transform (IDFT), see for example (Tan and Jiang, 2013)

$$x[t_n] = \sum_{h=1}^{N} X[\omega_h]e^{i\omega_h t_n} \tag{C1}$$

N is the total number of discrete frequency points within the bandwidth BW (Hz) considered. Angular-frequency points ω_h (rads^{-1}) and time points t_n (s) are calculated with the minimum- and maximum frequency of BW, f_{lo} and f_{hi} respectively (Hz) via

$$\omega_h = 2\pi\left\{[h-1]\left(\frac{f_{hi}-f_{lo}}{N-1}\right)+f_{lo}\right\} \qquad h = 1,2,3,...,N \tag{C2}$$

$$t_n = \frac{n-1}{f_{hi}-f_{lo}} \qquad n = 1,2,3,...,N \tag{C3}$$

Next the time-domain response $x[t_n]$ was multiplied by the time-domain filter, or gate, which was a block function of width τ_g whose sides fall off according to a rapidly decaying Gaussian function. The gate's start- and end times corresponded to the distances indicated in Fig. 4: $t_{sg} = 2r_{sg}/c$ and $t_{eg} = 2r_{eg}/c$ respectively. In this manner only the surface's scattering events of interest remained in the signal. Graphically, this is the intersection of depicted green ring of Fig. 4 and the scatterometer footprint A_{fp}. The gated signal $x[t_n]$ was then transformed back into the frequency domain via the Digital Fourier Transform (DFT)

$$X[\omega_h] = \frac{1}{N}\sum_{n=1}^{N} x[t_n]e^{-i\omega_h t_n} \tag{C4}$$

which then contains only the surface scattering information.

The frequency dependence of the radiation patterns, as shown in Fig. C1, complicates the process described above. The time-domain equivalent of the transmitted scatterometer signal is a pulse of width $\tau_p = 1/BW$ s. Depending on the angle with respect to boresight, i,e, α & β, this signal pulse will contain different frequencies, and will therefore have a different temporal shape. At greater angles α & β, high-frequency components of the pulse are not present causing the pulse to be broader there. As a result, the footprint area A_{fp}, which is determined from the (known) antenna radiation- or gain patterns G and the gate width $w_g = c\tau_g$ will become broader. By narrowing our bandwidths such that the radiation patterns of the frequencies within can be considered equal we avoided this issue. For the lower frequencies selected BW should be narrower than those for the higher frequencies. Used bandwidths were $BW = 0.5$ GHz for $2.5-3.0$ GHz, $BW = 0.5$ GHz for $4.5-5.0$ GHz and $BW = 1$ GHz for $9-10$ GHz. Note that there were additional considerations for picking these BW values, which are explained in Sec. 4.3.

However, when measuring the reference target backscatter response E_c (Vm^{-1}) the full $0.75 - 10.25$ GHz frequency range can be used. Because the solid angle extending the standard is small we may reasonably assume that all frequencies are present in the time-domain equivalent pulse at the standard, i.e. $G(\alpha, \beta) \approx 1$ for all frequencies. The benefit of using this broad bandwidth (9.5 GHz) is a high temporal/spatial resolution in the time domain, which allows for precise placement of the gate over the reference target response.
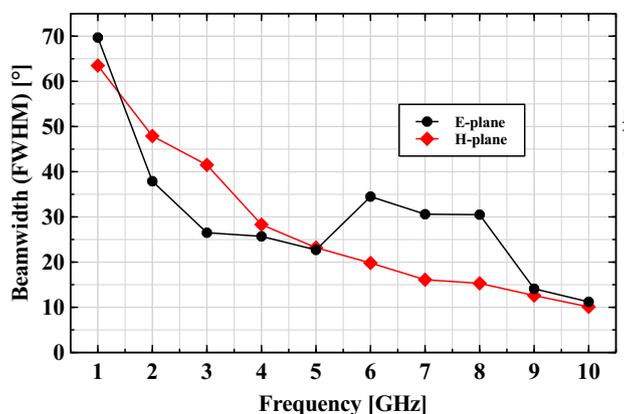
Figure C1. Beamwidths of dual polarization antennas. Shown is the full width half max (FWHM) of the measured radiation intensity patterns in the two principal planes (Schwarzbeck Mess-Elektronic, 2017).

Appendix D: Details on sources of measurement uncertainty

D1 Temperature-induced radar return uncertainty

The performance of the VNA's transmitters and receivers will vary due to variations of their operational temperatures, which in our case are directly linked to the temperature inside the VNA enclosure $T_{encl.}$. Many scatterometer systems employ a so-called internal calibration loop, see for example Ulaby and Long (2017), Baldi (2014), and Werner et al. (2010). This means that besides, or in between, scatterometer measurements the transmitter and receiver are connected, via a switch, trough a reference transmission line of fixed length that has a pre-determined attenuation and phase. This way, any fluctuations in the transmitter and/or receiver output over time can be measured and consequentiality removed from the target response. Instead of such an internal calibration loop we employ a different method to account for temperature-induced fluctuations of the VNA's transmitter and receiver performance.

During a half-day timespan the antennas were aimed at a fixed target at 21 m distance: the bare metal mast (without the pyramidal absorbers in front) with on top a metal sphere. At half-hour intervals the radar return was measured together with $T_{encl.}$. The fixed target was assumed to remain constant during that time, so any changes in the radar return were attributed to

the changing $T_{encl.}$, which varied from $25 - 35\ ^\circ\text{C}$ during the experiment.

For bandwidths at S-band ($2.5 - 3.0$ GHz), C-band ($4.5 - 5.0$ GHz), and X-band ($9.0 - 9.9$ GHz) the radar returns E_f (Vm^{-1}) (subscript f for 'fixed target') were filtered by a gate placed over the fixed target time-domain response, resulting in E_f^{fg} (superscript gf for 'gate over fixed target'). The change of E_f^{gf} over time t, and thus over $T_{encl.}$, is denoted $\Delta E_f^{gf}(T_{encl.})$:

$$\Delta E_f^{gf}(T_{encl.}) = E_f^{gf}(t) - E_f^{gf}(t = 0) \tag{D1}$$

In Fig. D1 the bandwidth-average results of $\Delta E_f^{gf}(T_{encl.})$ are shown over time alongside with $T_{encl.}$. There appeared to be no unique relationship between ΔE_f^{gf} and $T_{encl.}$. Within three hours from the experiment start $T_{encl.}$ increases to a maximum value after which it decreases again at an increasingly slowed rate. Also the curves $\Delta E_f^{gf}(T_{encl.})$, in general, change more rapidly over the first five hours and then become more stable. However, the direction of change in $T_{encl.}$: a rapid increase at the start, followed by a decrease after 19:15 at an increasingly slow rate is not seen in the $\Delta E_f^{gf}(T_{encl.})$ curves. So in order to
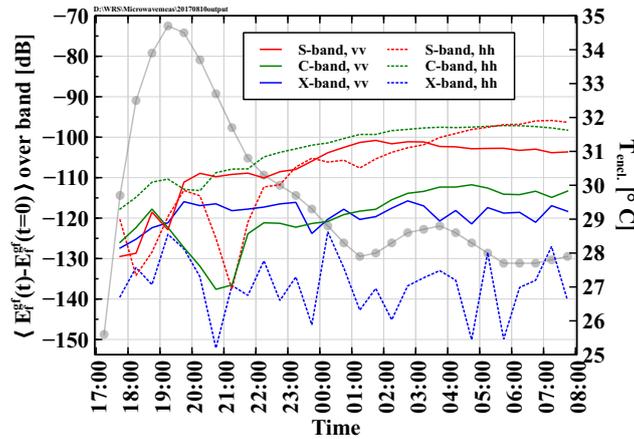
Figure D1. Measured radar return from a fixed target over a varying enclosure temperature $T_{encl.}$

quantify the temperature-induced VNA instability we used the maximum observed variation of $\Delta E_f^{gf}(T_{encl.})$ over time amidst all frequencies within the considered BW to calculate the temperature-induced radar return uncertainty ΔE_T^g (Vm^{-1}) as

$$\Delta E_T^g = \frac{max[\Delta E_f^{gf}(T_{encl.})] - min[\Delta E_f^{gf}(T_{encl.})]}{2} \tag{D2}$$

Table 4 lists ΔE_T^g values for the considered bandwidths and polarizations. ΔE_T^g is to be treated as an absolute uncertainty of E_e^g (Eq. 10) according to:

$$I_N = c\epsilon_0 \frac{1}{N} \sum_{i=1}^{N} (E_e^g(f_i) - E_n^g(f_i) \pm \Delta E_e^g)^2 \tag{D3}$$

D2 Reference target measurement uncertainty

The absolute backscattering coefficient is determined with respect to the known RCS of a reference target. Errors in the used reference target RCS itself, or errors made during the measurement of that target will contribute to the σ_0 uncertainty. The RCS

730 of a rectangular metal plate calculated with Eq. (B1) was found to match experimental observations fairly well (Ross, 1966), and therefore errors in the RCS of our rectangular plate itself were not considered. We did consider errors in the measurement of the reference target, specifically we considered misalignment of the scatterometer's antennas towards the rectangular plate and vice versa.

735 The angle of the rectangular plate with respect to the antenna boresight direction was estimated to be $-2.25° \le \beta_0 \le 1.25°$ in the horizontal direction and $-1.3° \le \alpha_0 \le 1.3°$ in the vertical direction. Given the large distance from the antennas to the rectangular plate, $R_c = 36.3$ m, and the much smaller separation between the transmit- and receive antennas, $W_{ant} = 0.4$ m, single uncertainty values $\Delta\alpha_0$, $\Delta\beta_0$ were used for both antennas. Due to this possible antenna misalignment the reference target is not illuminated by the peak value of the gain pattern, i.e. $G = G(\alpha_0 \pm \Delta\alpha_0, \beta_0 \pm \Delta\beta_0)$ $(-)$, resulting in an uncertainty

740 in the measured radar response of the reference target, and thus in K (Wm^{-1}). Eqation 8 then is modified to

$$K = c\epsilon_0 (E_c^{gc} - E_{bc}^{gc})^2 \frac{G(\alpha,\beta)^2}{G(\alpha_0 \pm \Delta\alpha_0, \beta_0 \pm \Delta\beta_0)^2} \left(\frac{R_c}{R_{fp}}\right)^4 \frac{A_{fp}}{\sigma^{bi}} \qquad (D4)$$

Alignment of the individual antennas with respect to the rectangular plate's surface normal was achieved with the help of a laser pointer mounted between the two antennas and a detachable mirror on the rectangular plate. The best alignment was found by rotating the plate until the reflected laser spot was on (or close to) the laser pointer again. In the horizontal plane,

745 the angle between the rectangular plate's surface normal and the transmit antenna was $0.15°$ (right side of the normal) for the transmit- and $-0.45°$ for the receive antenna. In the vertical plane, the angle between the rectangular plate's surface normal and both antennas (as they are next to each other) was close to zero. We estimated the uncertainty of aforementioned angles to be $\pm 0.10°$ both in the horizontal- and vertical plane. Starting with a model for the monostatic RCS of a metal rectangular plate, $\sigma(\theta,\phi)$ (Kerr, 1951) p. 457, a bistatic-RCS version $\sigma^{bi}(\theta_i, \phi_i, \theta_o, \phi_o)$ was created by considering a linear phase delay along

750 the plate's surface. Subscripts i refer to the incident wave direction and subscripts o to the observer's viewing direction. The calculation of K can then be extended to include the (mis)alignment of both individual antennas with respect to the rectangular plate's surface normal, and its uncertainty, by also inserting σ^{bi} into Eq. 8. We then obtain Eq. D4.

How the uncertainties $\Delta\alpha_0$, $\Delta\beta_0$ and the uncertainties in $\theta_i, \phi_i, \theta_o, \phi_o$ (not shown in Eq. D4) propagate into the uncertainty

755 of K, called the reference target measurement uncertainty ΔK, may be found in textbooks such as Hughes and Hase (2010). Resulting ΔK values, per considered BW and polarization, are presented as relative uncertainties in Table 4. With X-band the ΔK values are highest because the antenna radiation patterns are most narrow for higher frequencies.

D3 Noise floor and Noise Equivalent σ^0

760 The noise floor level of the radar return E_n^g (Vm^{-1}) per sub bandwidth was measured by aiming the scatterometer antennas skywards at $\alpha_0 = +35°$. The superscript g denotes that per bandwidth the same gating filter was applied as during the measurements of the ground target. The Noise Equivalent σ^0 (NES) $(\mathrm{m}^2\mathrm{m}^{-2})$ is the lowest possible value of σ^0 that can be measured

given E_n^g and the other scatterometer's parameters such as R_{fp} (m) and A_{fp} (m^2). The NES is calculated by assuming E_n^g as the radar return in Eq. 6. Table 4 summarizes the noise-floor levels and subsequent NES values per considered bandwidth and polarization. The higher NES level for S-band with hh polarization is attributed to a stronger interaction of the antenna's near-field radiation pattern with the tower features.

D4   Propagataion of uncertainties

In this section we demonstrate how Eq. 12 is derived. We show, using error-propagation theory, how each of the (three) error-terms ΔE_T^g, ΔK, and fading, propagates into an error for σ^0 and how all errors may be combined into one statistical confidence interval for σ^0. We start with Eq. 6, which with Eq. 9 can be written as

$$\sigma^0 = \frac{\bar{I}}{K} = \frac{I_N}{K(1 \pm 1/\sqrt{N})} \tag{D5}$$

The term between brackets in the denominator we may simply rewrite as $F \pm \Delta F$, i.e. a variable with an error. The variables I_N and K also have their respective errors ΔI_N and ΔK. When we write all variables and their errors explicitly we end up with

$$\sigma^0 = \frac{I_N}{KF} = \frac{I_N \pm \Delta I_N}{(K \pm \Delta K)(F \pm \Delta F)} \tag{D6}$$

We shall now describe all three error terms, starting with ΔI_N. The calculation of I_N from the measured backscattered electric field is given by Eq. D3 as

$$I_N = c\epsilon_0 \frac{1}{N} \sum_{i=1}^{N} (E_e^g(f_i) - E_n^g(f_i) \pm \Delta E_T^g)^2 \tag{D7}$$

with ΔE_T^g as measurement uncertainty. As explained in Sec. 4.3, every term in the above sum may be considered an independent variable. Because the number of samples N within BW is sufficiently large (about 15) we consider ΔE_e^T as a statistical error and therefore use the corresponding equation for error propagation (see for example Hughes and Hase (2010)) to calculate the total statistical error ΔI_N:

$$\Delta I_N = c\epsilon_0 \frac{2\Delta E_T^g}{N} \sqrt{\sum_{i=1}^{N} (E_e^g(f_i) - E_n^g(f_i))^2} \tag{D8}$$

ΔI_N can be considered as the one-standard-deviation value of I_N. Since the number of terms in the sum N are large enough we can consider $\pm \Delta I_N$ as the edges of a 66 % confidence interval for I_N.

As explained in Sec. D2 ΔK can be calculated by using error propagation theory for the errors $\Delta\alpha_0$, $\Delta\beta_0$ and those associated with the bistatic RCS of the rectangular metal plate. Note however that $\Delta\alpha_0$ and $\Delta\beta_0$ are maximum possible errors so the appropriate error propagation rules should be used. In order to have differentiable functions for the E-plane and H-plane antenna

gain patterns, $E_{patt}(\alpha_0)$ and $H_{patt}(\beta_0)$ respectively, the measured radiation patterns can be fitted with Gaussian functions for angles close to antenna boresight. Writing ΔK explicitly is straightforward.

Finally the error ΔF, which of course is $1/\sqrt{N}$. As explained in Sec. 4.2 this error represents a 68% confidence interval for $\bar{I}$.

795

Returning to Eq. D6 we now combine all three errors into one statistical error. To do so we must first convert ΔK from being a maximum possible error into a statistical error like ΔI_N and ΔF. This can be done by multiplying ΔK with 2/3, so the result may be interpreted as a one standard deviation value for K. This is equivalent to saying that $\pm 2/3\Delta K$ is a 68 % confidence interval for K. We combine the three statistical errors conservatively into a 66 % confidence interval for σ^0:

$$800 \quad \sigma^0 = \frac{I_N}{KF} = \frac{I_N \pm \Delta I_N}{(K \pm \frac{2}{3}\Delta K)(1 \pm 1/\sqrt{N})} = \frac{I_N}{KF} \pm \Delta\sigma^0 = \frac{I_N}{K} \pm \Delta\sigma^0 \tag{D9}$$

where Δ^0 is calculated according to the error propagation equation for statistical errors:

$$\left(\Delta\sigma^0\right)^2 = \left(\frac{\partial\sigma^0}{\partial I_N}\right)^2 (\Delta I_N)^2 + \left(\frac{\partial\sigma^0}{\partial K}\right)^2 (\Delta K)^2 + \left(\frac{\partial\sigma^0}{\partial F}\right)^2 (\Delta F)^2. \tag{D10}$$

References

Agilent: Time Domain Analysis using a Network Analyzer, application note 1287-12, Report, 2012.

805 Axline, R. M.: Experimental and Simulated Study of Scattering from Randomly Rough Surfaces, Thesis, 1974.

Balanis, C.: Antenna theory : analysis and design, Wiley Interscience, Hoboken, NJ :, 3rd ed. edn., 2005.

Baldi, C.: The design, validation and analysis of surface based S-band and D-band polarimetric scatterometers, Thesis, 2014.

Bansal, R.: The far-field; how far is far enough?, Applied Microwave and Wireless, 1999.

Clapp, R.: A theoretical and experimental study of radar ground return, Report, 1946.

810 De Porrata-Dória i Yagüe, R., Ibars, A. B., and Martínez, L. F.: Analysis and reduction of the distortions induced by time-domain filtering techniques in network analyzers, IEEE Transactions on Instrumentation and Measurement, 47, 930–934, https://doi.org/10.1109/19.744645, cited By :14 Export Date: 16 February 2017, 1998.

de Roo, R. D. and Ulaby, F. T.: Bistatic specular scattering from rough dielectric surfaces, IEEE Transactions on Antennas and Propagation, 42, 220–231, https://doi.org/10.1109/8.277216, 1994.

815 Dente, L., Ferrazzoli, P., Su, Z., van der Velde, R., and Guerriero, L.: Combined use of active and passive microwave satellite data to constrain a discrete scattering model, 155, https://doi.org/10.1016/j.rse.2014.08.031, 2014.

Dobson, M., Ulaby, F., Hallikainen, M., and El-rayes, M.: Microwave Dielectric Behavior of Wet Soil-Part II: Dielectric Mixing Models, IEEE Transactions on Geoscience and Remote Sensing, GE-23, 35–46, https://doi.org/10.1109/TGRS.1985.289498, 1985.

Famiglietti, J. S., Ryu, D., Berg, A. A., Rodell, M., and Jackson, T. J.: Field observations of soil moisture variability across scales, Water
820 Resources Research, 44, https://doi.org/10.1029/2006wr005804, 2008.

Fung, A., Liu, W., Chen, K., and Tsay, M.: An Improved Iem Model for Bistatic Scattering From Rough Surfaces, Journal of Electromagnetic Waves and Applications, 16, 689–702, https://doi.org/10.1163/156939302X01119, 2002.

Geldsetzer, T., Mead, J. B., Yackel, J., Scharien, R. K., and Howell, S. E. L.: Surface-Based Polarimetric C-Band Scatterometer for Field Measurements of Sea Ice, IEEE Transactions on Geoscience and Remote Sensing, 45, 3405–3416, https://doi.org/10.1109/TGRS.2007.907043,
825 2007.

He, Y., Guo, X., and Wilmshurst, J. F.: Comparison of different methods for measuring leaf area index in a mixed grassland, Canadian Journal of Plant Science, 87, 803–813, https://doi.org/10.4141/CJPS07024, 2007.

Hofste, J. and Su, Z.: Long-term Ground-based Broadband Microwave Scatterometer Observations of an Alpine Meadow over the Tibetan Plateau, https://doi.org/10.17026/dans-zc5-skyg, 2020.

830 Hofste, J., van der Velde, R., Wang, X., Zheng, D., Wen, J., van der Tol, C., and Su, Z.: Broadband Full Polarimetric Scatterometry for Monitoring Soil Moisture and Vegetation Properties Over a Tibetan Meadow, in: IGARSS 2018 - 2018 IEEE International Geoscience and Remote Sensing Symposium, pp. 2007–2010, Hofste2018, https://doi.org/10.1109/IGARSS.2018.8519380, 2018.

Hughes, I. and Hase, T.: Measurements and their uncertainties : a practical guide to modern error analysis, 2010.

Hwang, J., Kwon, S., and Oh, Y.: Evaluation of calibration accuracy with HPS (Hongik Polarimetric Scatterometer) system for multi-
835 bands and multi-polarizations, in: IGARS 2011 - 2011 IEEE International Geoscience and Remote Sensing Symposium, pp. 3987–3990, https://doi.org/10.1109/IGARSS.2011.6050105, 2011.

Jersak, B. D., Dolaty, M., and Blanchard, A. J.: Time domain enhancement of frequency domain radar cross-section data, International Journal of Remote Sensing, 13, 2105–2119, https://doi.org/10.1080/01431169208904256, cited By :2 Export Date: 16 February 2017, 1992.

840 Joseph, A. T., van der Velde, R., O'Neill, P. E., Lang, R., and Gish, T.: Effects of corn on C- and L-band radar backscatter: A correction method for soil moisture retrieval, Remote Sensing of Environment, 114, 2417–2430, https://doi.org/http://dx.doi.org/10.1016/j.rse.2010.05.017, 2010.

Kerr, D.: Propagation of Short Radio Waves, McGraw-Hill Book Company Inc., 1951.

Kim, Y., Jackson, T., Bindlish, R., Hong, S., Jung, G., and Lee, K.: Retrieval of Wheat Growth Parameters With Radar Vegetation Indices,
845 IEEE Geoscience and Remote Sensing Letters, 11, 808–812, https://doi.org/10.1109/LGRS.2013.2279255, 2014.

Kouyoumjian, R. G. and Peters, L.: Range requirements in radar cross-section measurements, Proceedings of the IEEE, 53, 920–928, https://doi.org/10.1109/PROC.1965.4070, 1965.

Kweon, S. and Oh, Y.: A Modified Water-Cloud Model With Leaf Angle Parameters for Microwave Backscattering From Agricultural Fields, IEEE Transactions on Geoscience and Remote Sensing, 53, 2802–2809, https://doi.org/10.1109/TGRS.2014.2364914, 2015.

850 Lin, C., Rommen, B., Floury, N., Schüttemeyer, D., Davidson, M. W. J., Kern, M., Kontu, A., Lemmetyinen, J., Pulliainen, J., Wiesmann, A., Werner, C., Mätzler, C., Schneebeli, M., Proksch, M., and Nagler, T.: Active Microwave Scattering Signature of Snowpack—Continuous Multiyear SnowScat Observation Experiments, IEEE Journal of Selected Topics in Applied Earth Observations and Remote Sensing, 9, 3849–3869, https://doi.org/10.1109/JSTARS.2016.2560168, 2016.

Liu, P. W., Judge, J., DeRoo, R. D., England, A. W., Bongiovanni, T., and Luke, A.: Dominant backscattering mecha-
855 nisms at L-band during dynamic soil moisture conditions for sandy soils, Remote Sensing of Environment, 178, 104–112, https://doi.org/https://doi.org/10.1016/j.rse.2016.02.062, 2016.

Lv, S., Zeng, Y., Wen, J., Zhao, H., and Su, Z.: Estimation of Penetration Depth from Soil Effective Temperature in Microwave Radiometry, Remote Sensing, 10, 519, 2018.

MacArthur, A., Robinson, I., Rossini, M., Davis, N., and MacDonald, K.: A dual-field-of-view spectrometer system for reflectance and
860 fluorescence measurements (Piccolo Doppio) and correction of etaloning, European Space Agenccy.

Miller, D.: The Tibetan Steppe, book section 8, Food and Agriculture Organization of the United Nations, Rome, http://www.fao.org/3/y8344e0f.htm#bm15, 2005.

Monakov, A. A., Vivekanandan, J., Stjernman, A. S., and Nystrom, A. K.: Spatial and frequency averaging techniques for a polarimetric scatterometer system, IEEE Transactions on Geoscience and Remote Sensing, 32, 187–196, https://doi.org/10.1109/36.285201, 1994.

865 Mätzler, C.: Applications of the interaction of microwaves with the natural snow cover, Remote Sensing Reviews, 2, 259–387, https://doi.org/10.1080/02757258709532086, 1987.

Nagarajan, K., Liu, P. W., De Roo, R., Judge, J., Akbar, R., Rush, P., Feagle, S., Preston, D., and Terwilleger, R.: Automated L-Band Radar System for Sensing Soil Moisture at High Temporal Resolution, IEEE Geoscience and Remote Sensing Letters, 11, 504–508, https://doi.org/10.1109/LGRS.2013.2270453, 2014.

870 Nandan, V., Geldsetzer, T., Islam, T., Yackel, J., Gill, J., Fuller, M., Gunn, G., and Duguay, C.: Ku-, X- and C-band measured and modeled microwave backscatter from a highly saline snow cover on first-year sea ice, Remote Sensing of Environment, 187, 62–75, https://doi.org/https://doi.org/10.1016/j.rse.2016.10.004, 2016.

Oh, Y., Sarabandi, K., and Ulaby, F. T.: An empirical model and an inversion technique for radar scattering from bare soil surfaces, IEEE Transactions on Geoscience and Remote Sensing, 30, 370–381, https://doi.org/10.1109/36.134086, 1992.

875 Peel, M. C., Finlayson, B. L., and McMahon, T. A.: Updated world map of the Köppen-Geiger climate classification, Hydrol. Earth Syst. Sci., 11, 1633–1644, https://doi.org/10.5194/hess-11-1633-2007, hESS, 2007.

Ross, R.: Radar cross section of rectangular flat plates as a function of aspect angle, IEEE Transactions on Antennas and Propagation, 14, 329–335, https://doi.org/10.1109/TAP.1966.1138696, 1966.

Schwank, M., Wiesmann, A., Werner, C., Mätzler, C., Weber, D., Murk, A., Völksch, I., and Wegmüller, U.: ELBARA II, an L-Band Radiometer System for Soil Moisture Research, Sensors, 10, 584–612, 2010.

Schwarzbeck Mess-Elektronic, O.: Radiation pattern BBHX 9120 LF antenna, https://doi.org/www.schwarzbeck.de, 2017.

Seneviratne, S., Corti, T., Davin, E., Hirschi, M., Jaeger, E., Lehner, I., Orlowsky, B., and Teuling, A.: Investigating soil moisture–climate interactions in a changing climate: A review, Earth-Science Reviews, 99, 125–161, https://doi.org/https://doi.org/10.1016/j.earscirev.2010.02.004, 2010.

Stiles, J. M., Sarabandi, K., and Ulaby, F. T.: Electromagnetic scattering from grassland-part II: measurement and modeling results, IEEE Transactions on Geoscience and Remote Sensing, 38, 349–356, https://doi.org/10.1109/36.823930, cited By :32 Export Date: 7 November 2016, 2000.

Su, Z., de Rosnay, P., Wen, J., Wang, L., and Zeng, Y.: Evaluation of ECMWF's soil moisture analyses using observations on the Tibetan Plateau, Journal of Geophysical Research: Atmospheres, 118, 5304–5318, https://doi.org/10.1002/jgrd.50468, https://agupubs.onlinelibrary.wiley.com/doi/abs/10.1002/jgrd.50468, 2013.

Su, Z., Wen, J., Zeng, Y., Zhao, H., Lv, S., van der Velde, R., Zheng, D., Wang, X., Wang, Z., Schwank, M., Kerr, Y., Yueh, S., Colliander, A., Drusch, M., and Mecklenburg, S.: Multiyear in-situ L-band microwave radiometry of land surface processes on the Tibetan Plateau, Nature Scientific Data, in preparation, 2020.

Tan, L. and Jiang, J.: Digital Signal Processing, Fundamentals and Applications, Academic Press, Waltham MA USA, 2 edn., 2013.

Ulaby, F. and Dobson, M.: Handbook of Radar Scattering Statistics for Terrain, Artech House Inc., Norwood MA, USA, 1989.

Ulaby, F. and Long, D.: Microwave Radar and Radiometric Remote Sensing, The University of Michigan Press, Ann Arbor, 4 edn., 2017.

Ulaby, F., Moore, R., and Fung, A.: Microwave Remote Sensing Active and Passive Vol. II: Radar Remote Sensing and Surface Scattering and Emission Theory, Addison-Wesley Publishing Company, Reading, Massachusetts, U.S.A., 1982.

Ulaby, F., Haddock, T., and Austin, R.: Fluctuation statistics of millimeter-wave scattering from distributed targets, IEEE Transactions on Geoscience and Remote Sensing, 26, 268–281, https://doi.org/10.1109/36.3030, 1988.

Vachaud, G., Passerat De Silans, A., Balabanis, P., and Vauclin, M.: Temporal Stability of Spatially Measured Soil Water Probability Density Function, Soil Science Society of America Journal, 49, 822–828, https://doi.org/10.2136/sssaj1985.03615995004900040006x, 1985.

Wang, Q. and Gogineni, S.: A numerical procedure for recovering scattering coefficients from measurements with wide-beam antennas, IEEE Transactions on Geoscience and Remote Sensing, 29, 778–783, https://doi.org/10.1109/36.83993, 1991.

Werner, C., Wiesmann, A., Strozzi, T., Schneebeli, M., and Mätzler, C.: The snowscat ground-based polarimetric scatterometer: Calibration and initial measurements from Davos Switzerland, in: 2010 IEEE International Geoscience and Remote Sensing Symposium, pp. 2363–2366, Werner2010, https://doi.org/10.1109/IGARSS.2010.5649015, 2010.

Zheng, D., van der Velde, R., Su, Z., Wen, J., Wang, X., and Yang, K.: Evaluation of Noah Frozen Soil Parameterization for Application to a Tibetan Meadow Ecosystem, Journal of Hydrometeorology, 18, 1749–1763, https://doi.org/10.1175/jhm-d-16-0199.1, 2017a.

Zheng, D., Wang, X., Van der Velde, R., Su, Z., Zeng, Y., Wen, J., Wang, Z., Schwank, M., and Ferrazzoli, P.: L-Band Emission of Soil Freeze-Thaw State in the Third Pole Environment, IEEE TGRS, 2017b.